UNIVERSITY OF CALIFORNIA SAN DIEGO

Indocyanine Green Modified Silica Shells for Colon Tumor Marking

A thesis submitted in partial satisfaction of the requirements for the degree of Master of Science

in

Chemical Engineering

by

Adrian Garcia Badaracco

Committee in Charge:

Professor Andrew Kummel, Chair
Professor Nisarg Shah
Professor Liangfang Zhang

2020

The Thesis of Adrian Garcia Badaracco is approved, and it is acceptable in quality and form for publication on microfilm and electronically:

Chair

University of California San Diego

2020

DEDICATION

I dedicate this dissertation to my family and friends. I have always been able to rely on them for support, no matter how difficult the situation. I especially would like to thank my parents, Ricardo and Carol, for their encouragement and boundless love. No amount of distance or financial difficulty has ever come in the way of their support for our family. I could not have completed this degree without them.

TABLE OF CONTENTS

LIST OF FIGURES

LIST OF TABLES

LIST OF SYMBOLS AND ABBREVIATIONS

3-Triethoxysilylpropylamine	APTES
Annular bright field	ABF
Computerized Tomography	CT
Computerized Tomography Colonoscopy	CTC
Deionized water	DI water
Diethylenetriamine	DETA
Electron energy loss spectroscopy	EELS
Ethylenediaminetetraacetic acid	EDTA
Food and Drug Administration	FDA
Full width at half maximum	FWHM
High-angle annular dark-field	HAADF
Hollow silica shells	HSS
ICG bound to HSS	ICG@HSS
Indocyanine green	ICG
Intratumoral	IT
Intravenous	IV
Mesoporous Silica Nanoshells	MSNs
Near infrared	NIR
Phosphate-buffered saline	PBS
Poly-L-lysine	PLL
Region of interest	ROI
Scanning electron microscope	SEM
Scanning transmission electron microscopy	STEM
Silicon dioxide	SiO_2
Tetramethyl orthosilicate	TMOS
Transmission electron microscopy	TEM
Trimethoxyphenylsilane	TMPS
Trimethyl borate	TMB

ACKNOWLEDGEMENTS

I would like to thank Dr. Andrew Kummel for giving me the opportunity to join his research group. Over the past several years, he has constantly supported my research, academic and professional pursuits. I can confidently say that without Dr. Kummel's support, I would not be where I am today.

I would also like to thank Dr. James Wang, Christopher Barback, Dr. Natalie Mendez, Ching-Hsin (Laura) Huang, Dr. Jian Yang, Dr. William Trogler, Dr. Sarah Blair and our other collaborators. Their support in my day-to-day activities and scientific guidance has been paramount to my success. All my knowledge and findings were based directly on their expertise and previous work, which they have shared selflessly with me.

Finally, I would like to acknowledge our collaborators, the Kim lab at University of Texas at Dallas. Their assistance in collecting high quality electron microscope data was crucial for the completion of the present work.

Chapters One, partially, and chapters Two, Three and Four, in full, were published in Applied Surface Science as follows: Garcia Badaracco A, Ward E, Barback C, Yang J, Wang J, Huang CH, Kim M, Wang Q, Nam S, Delong J, Blair S, Trogler W, Kummel A. "Indocyanine green modified silica shells for colon tumor marking." Applied Surface Science, 2020. Minor changes to the text and figures have been made.

Funding for my research came from the Emerging Technologies Continuing Umbrella of Research Experience (ET CURE), a National Cancer Institute sponsored program.

ABSTRACT OF THE THESIS

Indocyanine Green Modified Silica Shells for Colon Tumor Marking

by

Adrian Garcia Badaracco

Master of Science in Chemical Engineering

University of California San Diego, 2020

Professor Andrew Kummel, Chair

Marking of colon tumors for surgery is normally done using India ink, but it cannot be imaged below the tissue surface and there is evidence of serious complications such as abscess, intestinal perforation and inconsistency of injection. A novel infrared marker was developed using FDA approved indocyanine green (ICG) dye and ultrathin hollow silica nanoshells. Using a positively charged amine linker, ICG was electrostatically bound to the shell surface. This

electrostatic attachment was shown to be stable under biological conditions. For ultra-thin wall 100 nm diameter silica shells, a bimodal ICG layer of < 3 nm was formed. Conversely, for thicker walls on 2 μm diameter silica shells, the ICG layer was only bound to the outer surface and was 6 nm thick. *In vitro* testing of fluorescent emission showed the particles with the thinner coating were considerably more efficient, consistent with self-quenching in the thicker ICG coatings due to formation of energy traps. *Ex vivo* testing showed that ICG bound to the 100 nm hollow silica shells was visible under 1.5 cm of tissue. *In vivo* experiments demonstrated the ability of ICG bound to 100 nm silica shells to mark tumors accurately with no diffusion in tissue and remain visible for over 12 days.

CHAPTER ONE

Introduction

1.1 Preview

Cancer is not a single disease, but rather a wide range of diseases that are characterized by abnormal growth and proliferation of mutated cells. This abnormal growth often results in a tumor (a solid mass of tissue), except in the case of cancers of the blood.[1] Cancer is one of the most prevalent diseases worldwide, with almost 2 million new cases and 600,000 deaths per year in the United States alone.[2] Typical first-line treatments include surgical removal, radiation, chemotherapy and more recently immunotherapy and other advanced treatments.

Colorectal cancer, defined as a bowel cancer located in the colon or rectum, is one of the leading cancers in terms of deaths, second only to lung cancers.[2, 3] As shown in Figure 1.1, there are over 50,000 annual deaths due to colorectal cancer in the United States alone.[4] A summary of the treatment lifecycle for colorectal cancer is shown in Figure 1.2a. Initial diagnosis of colorectal cancer may be based on a screening or symptoms. This initial diagnosis is confirmed by testing for blood and stool or by performing a colonoscopy (insertion of a small camera into the colon, see Figure 1.2b). Regardless of the diagnosis route, surgical resection (removal of the tumor) is the most effective treatment for non-metastatic colorectal cancers.[5, 6] In most cases, pre-operative marking of the lesions is performed to aid the surgeon in identifying and removing the correct segments of the bowel. Sometimes these steps may be combined, for example, smaller polyps may be tattooed for longitudinal follow-up and/or removed during a screening colonoscopy.[3, 7, 8]

Because surgical resection is the most effective treatment for colorectal cancers, accurate marking and localization of the lesions during surgery is vital to a favorable prognosis. The present study focuses on the development of novel materials for pre-operative marking of small lesions in colorectal cancers.

1.2 Laparoscopic Resection

Laparoscopic surgery consists of the use of small narrow tubes (trochars) which are inserted into sub 1 cm incisions and manipulated by the surgeon from outside of the body. This results in smaller incisions and less blunt trauma from tissue displacement. An example of this procedure is shown in Figure 1.2c. By reducing the invasiveness of the procedure, Laparoscopic surgery tends to achieve superior outcomes and shorter recovery periods than open surgery.[9-13]

Despite its advantages over open surgery, the loss of tactile feedback during laparoscopic surgery requires precise pre-operative marking, especially in colorectal cancer cases where the surgeon may not have direct access to the lesions even through surgical instruments. All laparoscopic equipment provides a video feed to the surgeon, which allows for visualization of pre-operative tattoo markings and thus localization of tumors that may not be detectable visually.[12] In addition to a visible light feed, many laparoscopic instruments now offer a near infrared (NIR) camera and light source. The NIR spectrum is of particular interest for biological imaging because of its low auto-fluorescence, reduced scattering and enhanced tissue penetration compared to the visible light.[14] These developments in laparoscopic equipment has enabled use of fluorescent tracers and markers, such as indocyanine green (ICG).[15]

1.3 Tumor Localization and Pre-operative Marking

Locating small colon cancers intraoperatively can be both challenging and technically difficult. Small lesions can be particularly hard to locate because they are harder to see, harder to palp and may even heal and re-appear periodically.[7] When a surgeon fails to locate a lesion previously noted during pre-operative colonoscopy, they may resect a larger section of colon than required or resect the wrong section altogether.[16, 17] Incidence rates of complications due to localization errors have been reported to be as high as 15.4%.[5] To mitigate this risk, pre-operative marking of the tumor is commonly performed. The most popular method to mark tumors pre-operatively is endoscopic tattooing.[7-9, 11, 18-20] This method consists of placing a permanent tattoo on or around the site of the lesions using an endoscopic instrument. Although alternative methods do exist, most are less accurate than tattooing or have their own set of drawbacks.[7, 8, 18, 21] A summary comparison of tumor localization methods is presented in Table 1.1.

1.3.1 Intraoperative Colonoscopy

Intraoperative colonoscopy is a promising alternative but requires proper training and can be less accurate than tattooing because the colon is commonly air-inflated during surgery and thus may distend and change the shape. A recent retrospective study addressing intraoperative colonoscopy reported poor outcomes due to bowel distention in 9 out of 13 cases.[22] Other reports using more advanced techniques for intraoperative colonoscopy, such as insufflation with CO_2 instead of air, showed reduced complications, but require specialized equipment and proper surgeon training.[17] Another consideration is that lesions noted during diagnosis may heal by the time the procedure is performed and thus would not be possible to find with intraoperative colonoscopy.[7, 15, 23]

1.3.2 Computerized Tomography

Computerized tomography colonoscopies (CTC) is another common method to locate tumors. The main advantage of CTC is its non-invasive nature, which may reduce overall care costs when used as a first-line screening. However, this does not necessarily hold for pre-operative marking due to reduced accuracies.[24] The accuracies reported for CTC are considerably lower than that of other methods. Up to 20% of tumors may be missed, and of the located tumors, only 75% are accurately located during surgery.[7, 17] CTC scans also have a high radiation dose, up to ten times that of a chest X-ray.[25]

1.3.2 Endoscopic Clips

Endoscopic clips, usually made of coated metal alloys, may be placed on or around a lesion during endoscopy as a form of pre-operative marking. They are ultrasound sensitive and/or fluorescent, allowing for multiple localization methods.[7] Although multiple clips can be used for each lesion, there is a risk to the clips detaching from the site resulting in loss lesion identification and harm to the patient.[7, 22]

1.3.2 Tattooing

Endoscopic tattooing is considered the safest and most accurate method of pre-operative marking.[7-9, 18] There are various accepted tattooing techniques, but it is generally accepted that the safest and most successful method to mark tumors pre-operatively is to inject a small amount of dye into the submucosal layer 2-3 cm distal to the lesion.[7, 8]

The most widely studied tattooing agent is India ink. India ink is commercially available ink used for cosmetic tattooing as well as drawing. It is composed of carbon-black particles and additives suspended in an aqueous solution.[7] Because it is not a medical product, India ink requires filtration and dilution to be used in a medical setting.[21] Due to the lack of

standardization for India ink, there are conflicting reports on the dilution of the solution for effective identification.[18, 21] Recently, specialized medical versions of India ink have emerged, such as SPOT® (GI Supply, Inc.). While these products do not fundamentally change the applications of India ink, they do address some of the risks of India ink by standardizing the supply and preparation of the ink.[8]

Although India ink is established as a reliable way to mark lesions in the colon, there are reports of side effects including colonic abscess, intestinal infarction and intestinal perforation, with incidences of some as high as 14.3%.[26-30] Furthermore, imaging is restricted to the surface of tissues since India ink can only be imaged by visible light. In addition to the possible side effects related to use of India ink, there have also been reports of tattoo failure in up to 37% of cases.[9, 17] When these issues arise, they may lead to additional colonoscopies or even resection of the wrong section of the colon.[16, 17] These complications have led to the search for alternatives to India ink that might be safer and/or compatible with other imaging modalities, such as NIR.

In order to be a suitable replacement for India ink, dyes must have 4 distinct properties:

(1) High contrast and visibility.

(2) High biocompatibility.

(3) Chemical (temporal) stability: the material must not degrade significantly for at least two weeks (a typical timespan between marking and resection).

(4) Physical (spatial) stability: the material must not diffuse or be otherwise transported away from the injection site.

The only reported alternative tattooing agents are methylene blue and ICG. However, methylene blue has been shown to lead to many complications in addition to poor temporal

stability.[18] On the other hand, ICG is already widely used in medical setting and has a strong NIR fluorescence. The utility of ICG is limited due to its short lifetime (< 2 week).[7, 28, 31]. Loading ICG onto silica shells may improve this shortcoming.[32-34] Table 1.3 compares India ink, ICG dye and the ICG/silica hybrid materials presented in this study according to the four requirements highlighted above. Further details on ICG are presented below.

1.4 Indocyanine Green Dye

ICG has been proposed as an alternative tattooing agent.[7, 19, 20, 28, 31] ICG is a tricarbocyanine that has strong absorption and emission maxima at ≈ 780 and ≈ 820 nm, respectively.[35] This dye is the only NIR dye approved by United States Food and Drug Administration (FDA). Due to its low toxicity, it is extensively used for optical imaging applications in the clinic.[14, 36-39] The use of intraoperative ICG continues to grow as there are more commercially available laparoscopic and robotic systems have gained the NIR imaging capabilities.[15] ICG is also reported to be used for other medical applications, such as photoacoustic imaging, [40-42] photothermal [43-45] and photodynamic therapies. [46] Because of existing widespread use in surgery and its well-established safety profile, ICG dye could be a viable alternative to India ink for tattooing tumors.

Although ICG is cleared from circulation in <5 minutes when injected intravenously due to protein and phospholipid binding, [34, 47] it has been reported to persist for several days when administered as an intratumoral (IT) injection and can serve as a safe colonic tumor marker [19, 20, 28, 29, 31]. Despite these promising results ICG alone may be inferior to India ink because >40% of ICG markings are not visible after 2

weeks. [19, 20, 28, 31] Since ICG is a single molecule, it may diffuse through tissues or be reabsorbed and lose visibility, especially under visible wavelengths. ICG also suffers from low water solubility and self-quenching by aggregation[48, 49].

To overcome the disadvantages of low stability, ICG has been incorporated into polymeric or metal nanoparticles which prevent ICG from proteins binding and degradation in water [42, 44, 45, 49, 50]. Lee et al. reported a biodistribution study of the ICG bound mesoporous silica nanoparticles (MSNs). The surface of silica particles was pretreated with 3-aminopropyltrimethoxysilane and ICG molecules were bonded to the amine groups by electrostatic force. The binding of ICG and the primary amine was stable in a water solution with pH ranging from 3.0 to 10.0. [34]

1.5 Silica Nanomaterials

Nanoparticles and nanostructured materials have emerged as promising technologies in materials science due to their unique and tunable physical, chemical and biological properties. There are many ways to classify these materials, but one common distinction is to categorize them into organic (polymer or lipid based) and inorganic (based on metals or metal oxides) materials. Amongst the inorganic materials, silicon dioxide particles stand out due to their biocompatibility, ease of synthesis and well-understood surface chemistry.[36, 51-53]

An important consideration in selecting a biomaterial is toxicity, which is highly dependent on the surface properties (charge and functional groups) as well as particle size.[53] For this study, porous hollow silica shells synthesized via the sol-gel method on polystyrene templates were chosen due to their a size distribution and ease of synthesis. Previously, synthesis of such particles with a diameter ranging from 100 nm to 2 μm and the application of these silica

shells as ultrasound contrast agents has been reported.[52, 54-61] These shells have high biocompatibility and low tissue mobility.[52, 62]

1.6 ICG Coated Silica Nanoshells

A summary of ICG/silica materials is provided in Table 1.3. To date, no ICG-based biocompatible materials have been tested for pre-operative marking of tumors.

In the present study, ICG coated silica shells are presented as a tumor marking agent that overcomes some of the limitations of free ICG dye. By attaching thin ICG layers to hollow silica nanoshells, high fluorescent brightness and low tissue mobility are achieved. Although only a small improvement in temporal stability compared to free ICG dye for these novel ICG coated silica shells, they have been shown a safe usage profile, the ease of visualization even when injected under 1 cm of tissue, and the stable anchoring effects to the site of initial injection. Therefore, ICG coated silica shells are a promising adjunct or replacement to the standard India ink.

1.7 Acknowledgments

Chapters One, partially, was published in Applied Surface Science as follows: Garcia Badaracco A, Ward E, Barback C, Yang J, Wang J, Huang CH, Kim M, Wang Q, Nam S, Delong J, Blair S, Trogler W, Kummel A. “Indocyanine green modified silica shells for colon tumor marking”. Applied Surface Science, 2020.

1.8 Figures and Tables

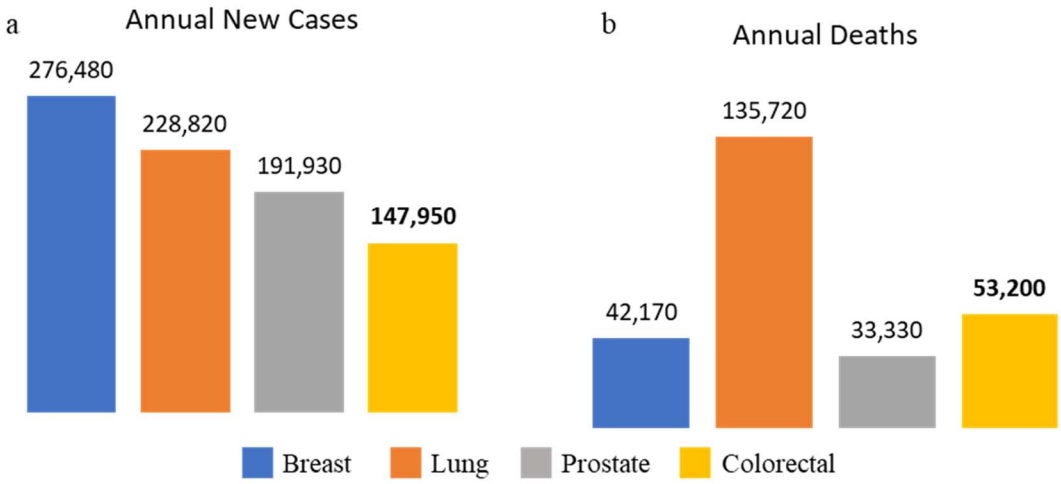

Figure 1.1 Estimated statistics of cancer mortality and incidence for the most common types of cancer in the United States in 2020. (a) Annual estimated incidence for the most common types of cancers. (b) Annual estimated deaths for the most common types of cancers. Colorectal Cancer is one of the leading cancers by death count, second only to respiratory cancers. Over 50,000 colorectal cancer related deaths are recorded each year.

Data from cancer.gov, *Cancer Stat Facts: Colorectal Cancer*.

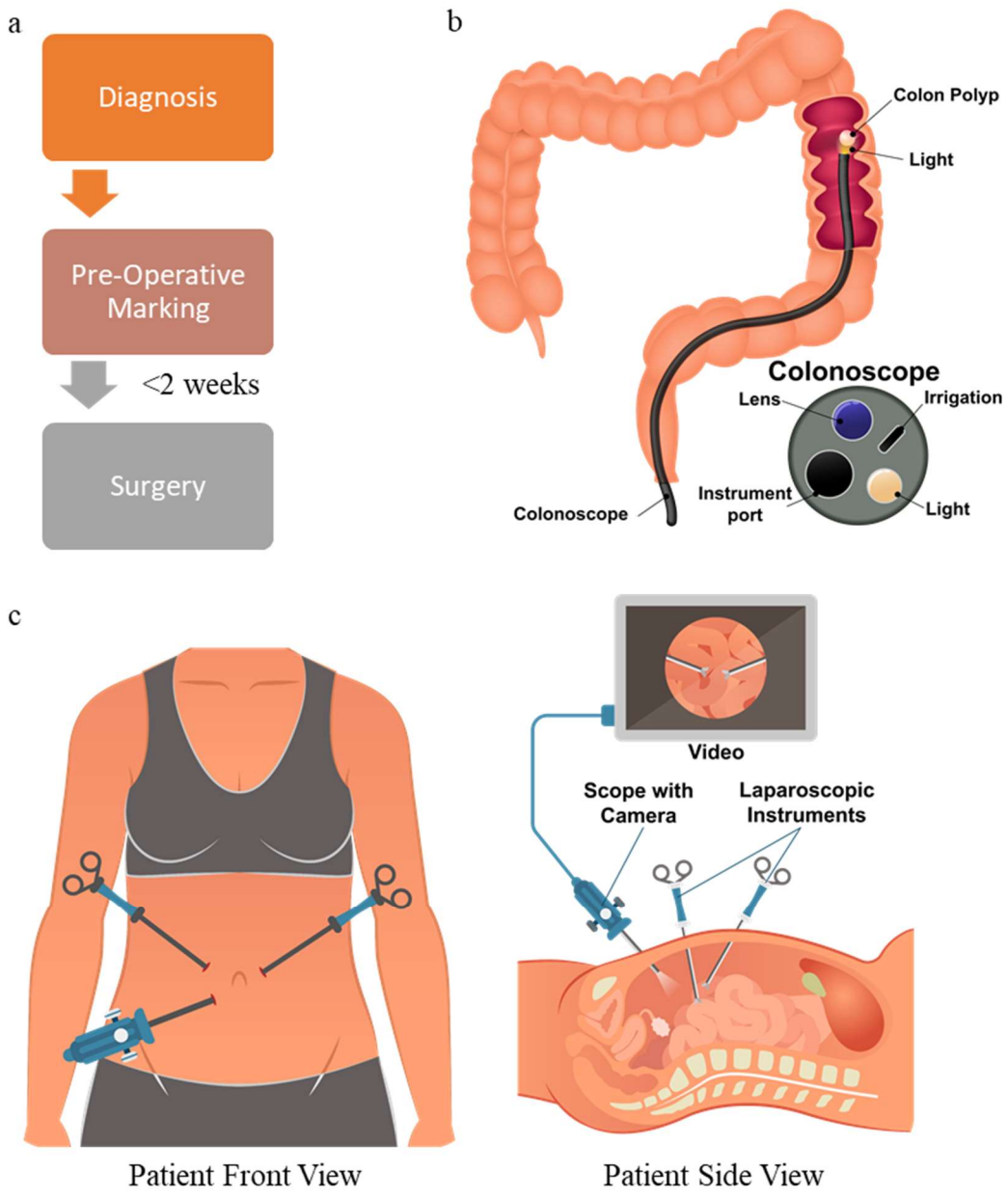

Figure 1.2 Colorectal cancer treatment lifecycle**.** (a) Typical colorectal cancer diagnostics cycle. Generally, diagnosis is followed by pre-operative marking and subsequent surgical resection. In some cases, pre-operative marking may be done concurrently with diagnosis or during a screening. (b) Example of a Colonoscopy. An endoscope (detail in top-right inset) is inserted into the anus and advanced into the rectum and colon. An onboard camera allows visualization of any lesions appearing in the colon. The colonoscope may also contain instrument ports that allow insertion of instruments to remove smaller polyps or tattoo lesions for tracking or surgical removal. (c) Example of a laparoscopic surgery. Several small incisions (ports) are made into the abdomen and thin tubes (trochars) containing surgical instruments and a camera are inserted. The surgeon then uses these instruments to manipulate tissue inside the patient.

Table 1.1 Comparison of pre-operative lesion marking techniques. Among the available techniques, tattooing stands out for pre-operative marking due to its extensive track record of relatively high accuracy as well as a relatively low rate of complications. CT colonoscopy stands out as the only non-invasive procedure. Finally, intra-operative colonoscopy offers high accuracy and is required in some cases if the surgeon finds new lesions not noted pre-operatively or if they are unable to find existing lesions, but there are concerns regarding surgeon training and bowel distension.

	Invasive?	Accuracy	Pros	Cons
Intraoperative colonoscopy	Yes	High	Less procedures Required in complex cases	Bowel distension
CT Scan	No	Low	Non-invasive	Expensive Radiation
Barium enema	Yes	Low	Lowest cost	
Clips	Yes	High	Multimodal imaging	Clips can fall off
Tattooing	Yes	High	Can be done during diagnosis	Complications from injection

Table 1.2 Comparison of ICG/silica systems. Although several silica/ICG particles have been synthesized, few have been tested for signal degradation in vivo, and none for tumor marking. Further, many formulations use small (<100 nm) particles or non-rigid particles, which might not be retained at the injection site. Finally, several procedures employ reagents have not yet FDA approved or involve complex synthesis, making in vivo clinical use challenging. Therefore, the novel aspect of this work lies in the application of biocompatible ICG loaded rigid particles to extend the viable ICG time for tumor marking.

	Delivery platform		Dye		In Vitro Signal Loss (24hrs) (no light)		In Vivo			
	Substrate	Size	Linking	Loading	Dye Protection		Injection	24hr Signal Loss	Notes	Ref.
ICG Coated Hollow SiO2 Shells	Ultrathin hollow SiO_2 shell	100 nm	ES	54 µg/mg	None	12% *	IT	4%	Followed 21 days	This study
Free ICG Dye	None	Molecule	N/A	N/A	N/A	24%	N/Q		In-vitro only	[63]
TEOS Capped MS SiO2/ICG Shell	MS SiO2 shell	30 nm	Trapped in matrix	77 µg/mg	SiO2	4%	N/Q		Developed for photodynamic therapy.	[33]
APTES Linked MS SiO2/ICG Shell	MS SiO2 shell	160 nm	ES	177 µg/mg	PEG	N/Q	N/Q		Developed for photodynamic therapy.	[61]
PEG Coated MS SiO2 / ICG	Solid MS SiO2	60 nm	ES	619 µg/mg	PEG	N/Q	N/Q		Shows improved photobleaching.	[64]
ICG / PEI in Hollow SiO2 Core	PEI in hollow SiO2	55 nm	ES	N/Q	Polymer	< 1%	N/Q		Toxic materials (PEI). No in vivo testing	[65]
SiO2/ICG coated Au Nanorods	MS SiO2 on Au core	44 nm	ES	N/Q	SiO2	N/Q	IT	N/Q	Visible in tumor 12hr after injection. Dye releases from particle over <2hr.	[66]
SiO2 / Polymer / ICG nanocomposites	Polymer / ICG on SiO2 core	80 / 120 nm	ES	23.6 µg/mg	Polymer	1 %	N/Q		Sophisticated polymer synthesis required.	[32]
MS SiO2/ICG Shell	MS SiO2	75 nm	ES	800 µg/mg	None	N/Q	IV	N/Q	Visible 90 min after injection.	[34]
ICG Doped Calcium Phosphate Nanoparticles	Calcium Phosphate Nanoparticles	16 nm	Trapped in solid	N/Q	PEG	N/Q	IV	N/Q	Visible after 96hr with some signal loss (by inspection of figures).	[67]
Micelle Protected ICG	Micelle	30 nm	Encapsulated	3.2 µg/mg	Polymer	0.25%	N/Q		Use of non-FDA approved materials.	[68]
ICG Liposome	Liposome	130 nm	Encapsulated	≈50 µM ICG 5 mM lipids	Lipid	1%	IV	N/Q	Visible 24hr after injection. Liposomes perfused into tumors.	[69]

*Calculated at 7 days
ES: Electrostatic
MS: mesoporous
PEI: Polyethylenimine
N/Q: not quantified
N/A: not applicable

Table 1.3 Comparison of tattooing agents**.** India ink stands out for its visible light imaging and stability. Indocyanine green (ICG) is highly biocompatible and has IR imaging capability but lacks chemical and temporal stability. Hollow silica shells (HSS) have good biocompatibility as well as temporal and spatial stability. This study seeks to evaluate the combination of ICG with HSS to create a marking agent with IR imaging capabilities and higher stability than pure ICG dye. Although HSS also have the possibility to enable multimodal imaging, this aspect was not tested in the present study.

	India ink	**ICG**	**HSS**	**HSS + ICG (this study)**
Biocompatible	+	++	+	Tested
Visible imaging	++	+	-	Not tested
IR imaging	-	++	-	Tested
Ultrasound imaging	-	-	+	Not tested
Temporal (chemical) stability	+	-	++	Tested
Spatial (location) stability	+	-	++	Tested

\+ good / high
++ very good / very high
\- not good / low

CHAPTER TWO

Materials and Methods

2.1 Preview

HSS were prepared in two sizes (100 nm and 2 μm). Briefly, silica shells are grown on a polystyrene template. The template is then removed by calcination, leaving a bare silica shell. ICG is then electrostatically linked to the shell, creating ICG/HSS. This mixture is then suspended in water and injected into tumor-bearing mice for in vivo studies or aliquoted for various in vitro experiments. A summary of the preparation of the shells is shown in Figure 2.1 and detailed below.

2.2 Materials

(3-Aminopropyl)triethoxysilane (APTES, CAS 919-30-2), indocyanine green (ICG, CAS 3599-32-4), N1-(3-Trimethoxysilylpropyl)diethylenetriamine (DETA, CAS 35141-30-1), tetramethyl orthosilicate (TMOS), trimethoxy(phenyl)silane (TMPS), Poly-L-lysine (PLL, CAS 25988-63-0) and solvents were purchased from Sigma-Aldrich (St. Louis, MO). Polystyrene templates were purchased from Polysciences Inc. (Warrington, PA).

2.3 Hollow Silica Shells

HSS were synthesized using methods previously reported. This procedure consists of self-assembling silica precursors on a commercially available polystyrene template. After the growth of a silica layer has been achieved, the particles were calcined to vaporize the polystyrene template, leaving a porous silica shell with a hollow core.[52, 54-61] Because of the synthesis of the shell is done on top of well characterized templates, the shells have a very narrow size distribution and

thus are very well suited for medical applications. [60, 61] Additionally, calcination of the particles for template removal ensures an inert and uniform surface free of residual reactants, resulting in lower toxicity than other synthesis methods.[70] This synthesis method is highly tunable, allowing for doping of the shell during or after growth to modify its physical or chemical properties.[52, 60, 71, 72] In the present study, 100 nm and 2 μm shells were used.

2.3.1 Synthesis of 100 nm Nanoshells

Synthesis of 100 nm nanoshells was done using a previously reported method. In brief, 50 mL of a 0.2% DETA solution was prepared by sonicating DETA in anhydrous ethanol for 5 minutes. Simultaneously, 430 mL of 95% ethanol was mixed with 2.5 mL of water and 6.25 mL of 100 nm polystyrene beads in a high sheer mixer at 4000 rpm to create a homogeneous suspension. 40 mL of the 0.2% DETA/ethanol solution was then added to the other components and the entire solution is mixed at 4000 rpm for 1 hour. After 55 minutes of mixing (5 minutes before the previous step concludes), silica precursor was prepared by vortexing 375 μL of TMOS and 500 μL of TMPS in 4 mL of ethanol. The precursor was then added to the polystyrene bead/DETA suspension and stirring at 4000 rpm was continued for another 5 hours. Removal of excess reactants was done by centrifugation at 3200 rpm for 25 minutes and subsequent washing with ethanol. The centrifuge/wash process was repeated at least twice. After overnight drying under ambient conditions, calcination was carried out with a 5 °C ramp up to 550 °C and then a constant step at 550 °C for 5 hours. [62]

2.3.2 Synthesis of 2 μm Microshells

The 2 μm microshells were synthesized similar to previously described protocols.[60, 72] First, 12 mL of phosphate buffered saline (PBS), 600 μL of polystyrene templates and 1680 μL of PLL were vortexed for 30 minutes in a 50 mL polypropylene tube. Then, 37.2 μL of TMOS

was added and vortexing was continued for another 2.5 hours. 15 minutes before the previous step concluded, a 2.5% TMB in ethanol solution was prepared by mixing 5 µL of TMB with 2 mL of absolute ethanol and vortexing for 15 minutes. Then, 600 µL of the TMB/ethanol solution was added to the polystyrene solution and vortexing was continued for an additional 5 hours. To remove excess reactants, deionized water washes (at least two) and then ethanol washes (at least 2) were performed. Calcination was identical to the 100 nm nanoshells but with an overnight period at 550 °C instead of 5 hours.

2.4 Indocyanine Green Coating

First, APTES was attached to the surface of the shells. APTES chemically bonds to the hydroxyl groups on the silica surface and provides a positively charged amine for the ICG anion to attach to. In order to graft APTES onto the surface of the silica nanoshells, 10 mg/mL of 100 nm or 2 µm silica shells suspended in ethanol were mixed with APTES to form a 1% v/v APTES/ethanol solution and then vortex mixed for 24 hours. Amine modified silica shells were subsequently washed twice with ethanol and twice with water to remove unbounded APTES.

To coat the silica shells with ICG, the amine modified 100 nm or 2 µm silica shells were resuspended at 10 mg/mL in a 10 mg/mL ICG water solution (ICG to silica shell ratio of 1:1 by mass) and vortex mixed for 5 hours at room temperature shielded from light. The ICG coated silica shells were collected by centrifuging for 5 minutes with 5000 rpm. The pellet was washed at least three times with water or until the solution was colorless. The green silica shells were then re-suspended in water at 20 mg/mL. These samples were kept at -20C and shielded from light until ready for use.

2.5 Quantification and Imaging of Dye Layer

Quantification of ICG on the silica shells was performed by measuring the absorption of ICG coated silica shells in water at 780 nm on a Perking Elmer Lambda 35 UV-Vis Spectrophotometer. In order to release the dye from the shells, the ICG coated shells were suspended in a 1% Tween20 solution as previously described by Hong et al.[61] The standard curve was made with the absorption of ICG water solution as a function of ICG concentration. When the absorption of ICG coated silica shells in water was measured, non-modified silica shells in water suspension at the same concentration of measured sample were used as a blank. Measurement of fluorescence intensity was performed using an NIR camera (Fluobeam-800, Fluoptics, Grenoble, France) at a distance of 15 cm.

Combined field emission SEM (FESEM) images were obtained using a Sigma 500 FE-SEM (Zeiss, Germany) with an accelerating voltage ranging from 0.8 to 20 kV. SEM samples were prepared by depositing silica shells on a carbon tape substrate.

Transmission electron microscopy (TEM) and scanning transmission electron microscopy (STEM) characterization are performed using a spherical aberration (Cs) corrected JEM-ARM200F electron microscope (JEOL USA INC) operated at 200 kV. The convergence semiangle of the electron probe is set to 25 mrad and the current of the electron probe is 23 pA. High angle annular dark field (HAADF) and annular bright field (ABF) imaging is carried out with the collection semiangle from 70-250 mrad and 12-24 mrad, respectively. Electron energy loss spectroscopy (EELS) is performed using an Enfina spectrometer (Gatan Inc.) with the collection simiangle of 30 mrad. 0.2 s/pixel is used for the elemental mapping of C and O using EELS. Quantification of layer thickness in Figure 3.5 and Figure 3.7 was performed using

MATLAB. Upscaling and a gaussian blur were applied before final quantification in order to remove the high noise visible in Figure 3.6.

2.6 Ex Vivo Phantom Testing

100 nm ICG coated shells were diluted to 0.25 mg/mL in DI water and 2 mL of this suspension was placed under a NIR camera at a standard distance of approximately 15 cm. Then, several layers of chicken or beef tissue were placed on top of the samples, mimicking injections at varying depths. After all the tissue layers were stacked, the sample was removed, and background images were taken. All images were taken using a fixed exposure time of 200 ms.

After background subtraction was performed, mean intensity of the sample area was measured. All statistical analysis and plotting were performed with Microsoft Excel and MATLAB while intensity measurements were performed using ImageJ.

2.7 In Vivo ICG Marked Tumor Imaging

All animal studies were approved by UC San Diego Institutional Animal Care and Use Comtee (IACUC). Single flank tumors were established in five C57 wildtype mice with GL261 cell line. To establish these tumors, $1x10^6$ cells were subcutaneously injected into the flank of anesthetized mice and allowed to grow for about two weeks to achieve an average of 217 mm^3 tumor volume. Tumors were injected with 25 μL of 20 mg/mL 100 nm ICG particles or equivalent free ICG at about 0.25 - 0.5 cm depth. Serial images of the tumor were taken on post-injection days 3, 5, 7, 10, 13, 15, 18 and 21. Mice injected with

ICG coated shells and free ICG dye were imaged on the same schedule and using a single-blind protocol. A summary of the imaging and analysis protocol for these experiments is shown in Figure 2.2.

2.8 In Vivo Toxicology

Healthy 6-8-week-old female BALB/c mice (n=3) were intravenously injected with 150 mg/kg plain 100 nm SiO_2 nanoshells to measure systematic toxicity. 24 hours after injection, 400 μL of blood was collected and put into tubes pre-coated with ethylenediaminetetraacetic acid (EDTA) as an anticoagulant. The tubes were immediately flicked and inverted several times to distribute the EDTA/blood and then analyzed using a Hemavet 950FS cell counter (Drew Scientific Inc., Miami Lakes, USA). All samples were measured twice in duplicate.

2.9 Acknowledgments

Chapters Two, in full, was published in Applied Surface Science as follows: Garcia Badaracco A, Ward E, Barback C, Yang J, Wang J, Huang CH, Kim M, Wang Q, Nam S, Delong J, Blair S, Trogler W, Kummel A. “Indocyanine green modified silica shells for colon tumor marking”. Applied Surface Science, 2020. Minor changes to the text and figures have been made.

2.10 Figures and Tables

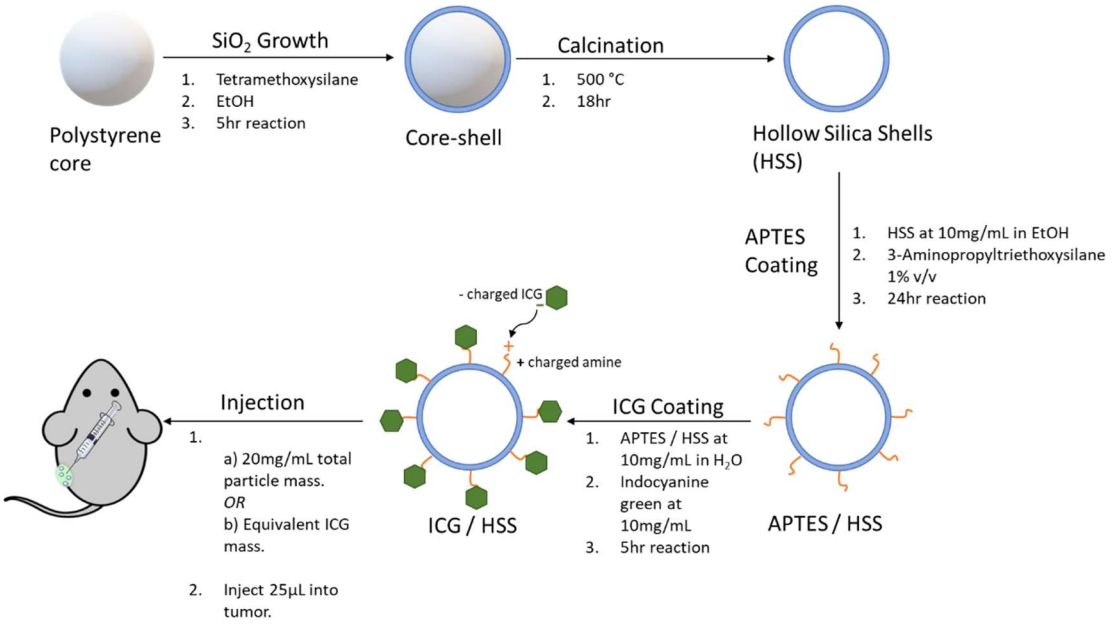

Figure 2.1 Preparation of ICG coated HSS**.** First, a polystyrene core was covered with a thin layer of silica to yield a core-shell structure as described in Ref. 34. Second, calcination was used to remove the sacrificial polystyrene core to produce a plain ultrathin hollow silica shell (UHSS). Third, to coat with ICG, UHSS were suspended at 10 mg/mL in pure ethanol and 10 µL of APTES was added (1% v/v). This solution was shaken vigorously for 24 hrs, followed by 2 washes with ethanol and 2 washes with water to remove any unreacted APTES. Fourth, 10 mg of ICG dye were added to this solution and shaken for 5 hours to yield ICG-loaded UHSS (ICG/HSS). The resultant ICG/UHSS were purified by washing with water until the supernatant was colorless. Fifth, tumor injections were performed with either 25 µL of a 20 mg/mL suspension of ICG/HSS in water or 25 µL of the ICG control in water with the same total ICG concentration.

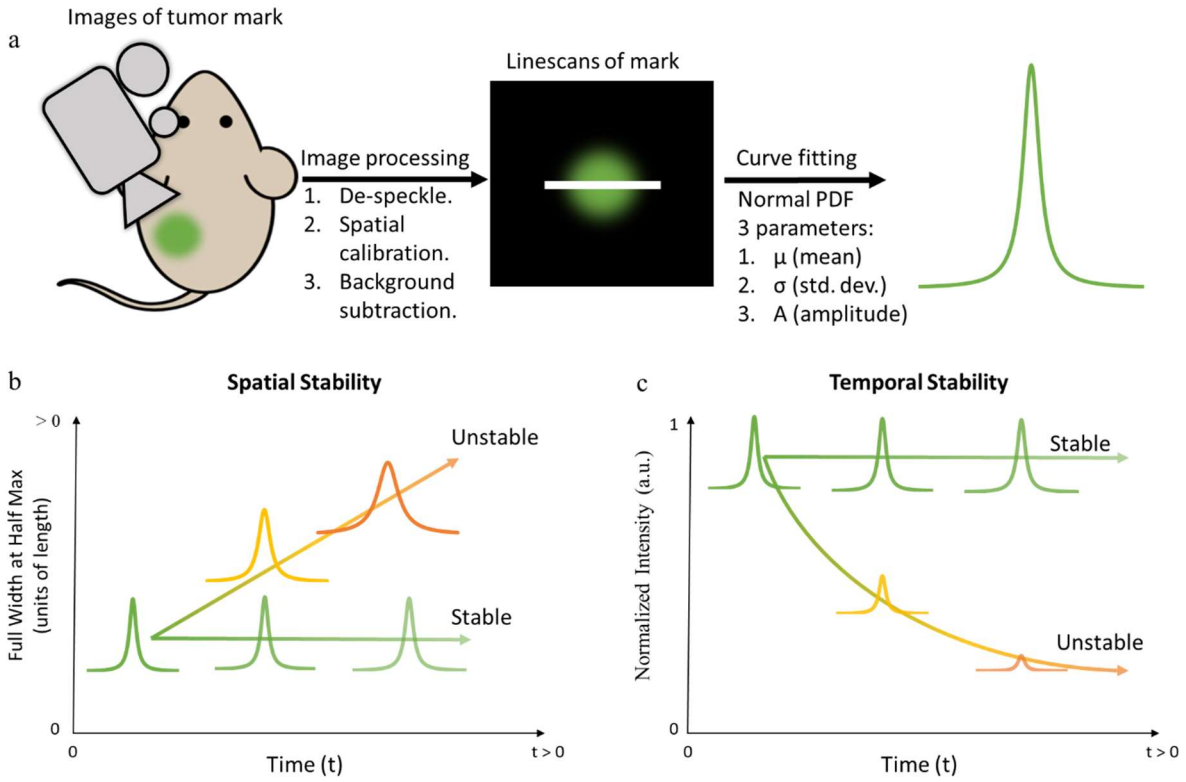

Figure 2.2 *In-vivo* measurement of spatial and temporal stability**.** (a) Schematic of data capture and processing. First, NIR images of tumor marks are taken and processed to remove artifacts and calibrate background intensity. Then, linescans of the tumor mark site are taken. In cases where the mark is too dim to find, its location is estimated based on brightfield images and existing data. Finally, these linescans are fit to a Normal distribution, resulting in 3 parameters (mean, standard deviation and amplitude). This process is repeated at different time periods over the course of two weeks. (b) The standard deviation (in the form of full width half max) is used to study the spatial stability of the mark. (c) The amplitude is used to study the temporal stability.

CHAPTER THREE

Results and Discussion

3.1 Electron Microscope Imaging of Shells

The general appearance of bare HSS is shown in Figure 3.1. Both 100 nm nanoshells and 2 μm microshells have thin walls and a hollow central cavity. For the 100 nm shells, the SEM image (Figure 3.1a) shows the shell diameters to be uniform and consistent across a large population of nanoshells. Figure 3.1b shows TEM images of the 100 nm nanoshells. For the 100 nm nanoshells, the wall thickness appears to be non-uniform relative to the diameter of the particle, consistent with a porous self-assembled shell. The shell walls appear dark due to high density SiO_2 in the wall while the interior of the shells appears translucent due to the hollow nature of the core. Figure 3.1c shows SEM images for the 2 μm HSS. The 2 μm microshells appear to have a thicker walls than the 100 nm nanoshells, but they appear uniform relative to the 2 μm shell diameter. Figure 3.1d shows TEM images for the 2 μm microshells and highlights the very thin walls relative to the diameter of the particles. Although the 2 μm hollow SiO_2 shells have thin and smooth walls, a small amount of colloidal silica is observed on the shells, appearing as small white spheres in the SEM image (Figure 3.1c) and darker spheres or aggregates in the TEM image (Figure 3.1d) adhered to the outside of the shell. These observations indicate that both 100 nm nanoshells and 2 μm microshells are of uniform diameter and consist of a thin silica wall with a hollow interior space.

Figure 3.2 shows TEM images of the silica shells with and without ICG. The panels on the left show TEM images of bare or ICG coated silica shells, while the panels on the right give a schematic diagram of the layers observed on TEM to assist in data interpretation. Schematics all correspond with the image directly to their left. Figure 3.2a shows an uncoated 100 nm nanoshell with a wall thickness of about 8 nm. As seen in the schematic of Figure 3.2b, this is a single SiO_2 layer encapsulating the hollow core of the particle. Figure 3.2c is an ICG coated 100 nm nanoshells. Here the wall thickness is seen to increase to 10 nm, and the additional ≈ 2 nm of wall thickness compared to the uncoated 100 nm particle is attributed to the ICG coating. Initially, this coating was assumed to be a single exterior coating, as depicted in Figure 3.2d but elemental mapping shown below is more consistent with a bilayer.

This comparison process is repeated for the 2 μm microshells. In Figure 3.2e, the uncoated 2 μm microshells have a wall thickness of 24 nm. As per the schematic in Figure 3.2f, the wall is composed of a solid 24 nm SiO_2 layer encapsulating the hollow interior space, although in the TEM image it can be observed that the SiO_2 layer may have regions of higher and lower density (based on the darkness of the shell) as well as large colloidal particles, like the ones seen in the top right of Figure 3.2e [60]. Once coated with ICG, the wall thickness of the 2 μm microshells increases to 27 nm, as seen in Figure 3.2g. The additional ≈ 3 nm is again attributed to a single ICG layer on the exterior of the particles. The thickness of this layer was reconfirmed by elemental mapping using TEM-EELS. This data, discussed in Section 3.4, confirms that both particles have a nanoscale ICG coating grown on the surface of the silica shell, with the 2 μm microshells having a slightly thicker coating than the 100 nm nanoshells.

3.2 In Vitro Chemical Stability

In order to explore the chemical stability of ICG electrostatically attached to silica nanoshells, the ICG coated silica shells were suspended in either pH 4.0 and pH 10.0 buffer overnight at room temperature and no free ICG molecules were found in the supernatant after spinning down the silica shells (data not shown) indicating that the combination of ICG and amine group is a strong bond and is stable in under physiological conditions. Long term chemical stability in water was also tested (Figure 3.3). ICG electrostatically attached to silica showed a slightly extended lifetime, with a $t_{1/2}$ of 56.4 h^{-1} for ICG/HSS compared to 16.6 h^{-1} for free ICG dye. The value for free ICG dye is in agreement with existing literature.[50, 73]

3.3 In Vitro Spectroscopic Analysis

An evaluation of in vitro brightness is shown in Figure 3.4. In Figure 3.4a, dye loading for 2 μm microshells and 100 nm nanoshells are compared. The loading of ICG on silica shells was calculated to be at minimum 54 μg/mg for 2 μm microshells and 43 μg/mg for 100 nm nanoshells?. This method has previously been shown to allow order of magnitude measurement of heterogenous ICG dye concentrations but underestimates loading due to absorption quenching.[61] Because the measured dye loadings are within 20% of each other, comparison between the two size of particles by on the basis of total mass concentration instead of ICG dye concentration is reasonable. Thus, all further experiments were performed controlling for total mass instead of ICG dye concentration or mass.

To compare the emission intensity of the shells, they were suspended at 0.25 mg/mL and 0.025 mg/mL (mass of SiO_2 / volume of DI water) and imaged using a NIR CCD camera. Two comparisons were made: differences in brightness between particle sizes are shown in Figure 3b and 3c while changes in brightness due to concentration are shown in Figure 3.4 d and e. Raw images from which the values are calculated are shown in Figure 3.5. The intensity values are mean intensity within a region of interest (ROI) while error bars represent standard deviations of intensity within ROI. Figure 3.4b shows that at 0.25 mg/mL, 100 nm nanoshells are 10x brighter than 2 μm microshells, while Figure 3.4c indicates that at a lower concentration of 0.025 mg/mL, 100 nm nanoshells are only 5x brighter than 2 μm microshells. In order to explore the non-linear difference in brightness, samples of the same size silica shell are compared. Figure 3.4d shows that 2 μm microshells increase in brightness 5x with a 10x increase in concentration, which is indicative of inter-particle self-quenching occurring at 0.25 mg/mL if not at both concentrations. For the 100 nm nanoshells, Figure 3.4e indicates a linear scaling of emission intensity with concentration within the 0.025 mg/mL and 0.25 mg/mL range, suggesting that interparticle self-quenching is not present for the 100 nm nanoshells but interparticle self-quenching is present for the 2 μm microshells (Figure 3.4d). Thus, despite similar dye mass loading, the 100 nm nanoshells were found to be significantly brighter than the 2 μm microshells at all concentrations. The 2 μm microshells seemed to suffer from severe self-quenching. In order to better understand the underlaying cause for this difference, TEM-EELS elemental mapping of the dye distribution on the shell walls was performed.

3.4 Elemental Analysis of Shell Wall

Figure 3.6a indicates the region used for TEM-EELS mapping inscribed by a blue rectangle on a TEM image of a nanoshells. Figure 3.6b is the TEM-EELS mapping of this region for carbon, which is expected to reflect the location of the ICG coating. Figure 3.6c shows the oxygen elemental mapping, which reflects the location of the SiO_2 shell wall. The carbon signal appears to be on both sides of the shell wall and is non-uniform. In order to quantify these maps, multiple linescans were taken across an area with a width ≈ 9 nm in the center of the images in Figures 3.6b and 3.6c. An example of a linescan for a single pixel is shown in Figure 3.7, confirming the same general trend seen for the area scan. This linescan area is represented by a white bar. The averaged linescans for carbon are presented in Figure 3.6d. Layer thickness was measured as the full width at half max (FWHM) of each peak after subtracting the background from the peak height. The carbon has a bimodal distribution, with a 2.6 nm layer on the exterior of the shell wall and a 0.9 nm layer on the interior of the shell. The minima between the carbon © peaks corresponds to the maxima of the oxygen (O) peak (Figure 3.6e). The data is consistent with formation of an inner ICG coating as well as an outer ICG coating. Since protein binding is known to cause quenching of ICG in vivo, the shielding of the internal ICG layer in the 100 nm nanoshells could extend the useful imaging lifetime when injected into blood or serum rich tissues. [34, 47, 61]. Additionally, the near monolayer coatings of dye found on the 100 nm nanoshells as well as their separation by an 8 nm silica shell results in a lower localized dye concentration, which has been shown to reduce the formation of energy traps (aggregates of dye molecules that decay absorbed energy non-radiatively) and thus limit self-quenching. [74, 75] Previous studies with higher ICG dye loading than the present nanoshells and microshells

have shown a that increasing localized ICG concentration on shells results in severe self-quenching.[61] This explains the strong fluorescence seen in Figure 3 for 100 nm nanoshells, since these have two very thin layers of ICG and there are few energy traps and thus self-quenching is minimized.

Figure 3.8 presents the TEM-EELS elemental mapping for the 2 μm microshells. Figure 3.8a shows a TEM image of the shell wall with the elemental mapping area enclosed by a blue square. In order to avoid possible complications from imaging through a shell too thick on the plane of the beam, mapping was performed on a broken microshell. The contour of the opening can be seen as a discrete change in contrast on the right side of the microshell. Figure 3.8b shows the elemental mapping of C on the 2 μm microshells. A single discrete layer of carbon is visible, located on the outside of the shell. On the right side of the shell, the layer seems to become more diffuse, likely due to imaging at the edge of the shell breakage, as highlighted in Figure 3.8a. Since this region was outside the analyzed area, it did not affect the results. Figure 3.8c shows the oxygen elemental mapping, which reflects the location of the SiO_2 shell wall. The averaged linescan shown in Figure 3.8d reflects the unimodal distribution of carbon on the 2 μm microshells with a single 6.1 nm exterior ICG layer. The ICG layer overlaps with the shell slightly, consistent with attachment to less dense silica layers which have previously been shown to be on the exterior of the shell.[60] Figure 3.8e shows the averaged linescans for oxygen. Previously, the for 2 μm microshells were shown to have a low density flaky exterior silica layer and a denser inner layer.[60] The gradual rise of the O signal is consistent with the shell becoming denser towards the center of the particle. The ICG dye can penetrate the less dense exterior silica layer, but not the whole thickness of the shell. The 2 μm microshells have much thicker shell walls (24 nm vs 8 nm for the 100 nm nanoshells), and thus ICG dye is not able to reach the hollow space. The formation

of a single thicker layer on the exterior of the 2 μm microshells results in a much higher probability of the creation of energy traps and thus explains the strong self-quenching seen in the emission tests of Figure 3.4. [61, 74, 75]

3.5 Imaging Penetration in Tissue

Tumor resection margins are typically about 1 cm; therefore, imaging of fluorescent dye marker injections 1 cm deep in tissue is often required. This also enables the surgeon to see the mark even when it is covered by other tissues. To evaluate penetration through tissue, ICG coated nanoshells were suspended in DI water at 0.25 mg/mL and covered with several layers of chicken or beef tissue. Each additional layer (average thickness of 5 mm for both beef and chicken) represents a step (Δx) increase in imaging depth. The distance between the NIR camera and the sample was fixed at $\approx$ 15 cm.

A schematic representation of this experimental setup is shown in Figure 3.9a. Figure 3.9b shows the decrease in intensity of the emission (normalized to the emission of uncovered ICG coated nanoshells) as imaging depth increased. All images were captured at 200 ms exposure. The intensity decay, shown in Figure 3.9b, corresponds to an exponential decay, with a faster decay in optically denser beef tissue than chicken. Under chicken breast, emission was clearly visible up to $\approx$ 1.5 cm while under beef tissue, the emission was visible up to $\approx$ 1 cm. Thus, ICG coated nanoshells are expected to be visible under up to 1 cm of tissue under clinically relevant imaging conditions, ensuring the ability of the surgeon to accurately mark sub-surface tumors. Sample images used to generate the plots in Figure 3.9b are shown in Figure 3.10.

3.6 Spatial Stability

One potential advantage of ICG coated shells over free ICG dye is reduced leakage through tissue. To test the spatial stability of ICG coated silica shells, the brighter 100 nm nanoshells and equivalent concentration (by mass of ICG) of free ICG dye were injected into tumor bearing mice. Tumors were grown at depths of 0.25 to 0.5 cm and the injected nanoshells were easily visible at these injection depths. Due to limitations in the animal model, tumors at larger depths were not tested.

The brightness of the tumor mark was imaged under the NIR camera at days 0, 3, 7, 10, 13, 15, 18 and 21. For each image, the emission profile was fitted to a Cauchy probability distributions function to quantify the change in emission profile with time. Only images from days 0, 3, 7 and 10 were fit because after this the signal was not bright enough to reliably fit the probability distribution function in some of the mice, particularly those with free ICG dye.

Figure 3.11a shows a visible light image of the experimental setup used for NIR imaging. Tumor bearing mice that were previously injected with either free ICG dye or ICG coated nanoshells are anesthetized and placed at a standard distance from the NIR camera. Images are captured at several exposures using NIR illumination and imaging as well as a single visible light image used to calibrate dimensions and locate the tumor in dim NIR images. Figure 3.11b shows the emission and fitted emission profile for a free ICG dye mark 10 days after injection. Although the injection site can still be distinguished, the emission appears broad, indicative of diffusion of the dye through tissue. Fit to a Cauchy distribution is plotted as a white dotted line (enlarged for viewing, not to scale) and reveals an average FWHM of over 1 cm for free ICG dye. Figure 3.11c

shows the emission for ICG coated nanoshells. The emission from the nanoshells is brighter and narrower, allowing immediate and precise localization of the injection site. Fit to a Cauchy PDF (shown as a dotted white line, not to scale) reveals an average FWHM of 0.4 cm for ICG coated nanoshells.

The change in emission profile over time is shown in Figure 3.11d. After 10 days, the emission profile of the ICG coated nanoshells remained unchanged and is considerably narrower than the emission profile of the free ICG dye ($p<0.05$). For free ICG dye, diffusion through tissue results in loss of precision as a tumor marking agent if surgical excision is not performed within a few days of marking. On the other hand, ICG coated nanoshells did not exhibit diffusion through tissue and their emission remained anchored to the site of injection up to 10 days after initial delivery.

3.7 Temporal Stability

Raw intensity of emission was also compared between days 3 and 21 and is plotted in Figure 3.12. Figure 3.12a shows that ICG coated nanoshells are significantly brighter than free ICG dye between day 7 and 15 ($p<0.05$), although there is a decay in signal for both groups towards day 21. This decay in signal was unexpected of the ICG coated nanoshells but is correlated with physiological progression of the tumors. As shown in Figure 3.13c, the tumors that grew rapidly lost NIR fluorescent signal. This would not be expected to occur in patients since human tumors usually take months or years to grow, as opposed to <2 weeks in this animal model. Future studies will be needed to test on a slower growing tumor model.

3.8 In Vivo Toxicology

Complete blood count (CBC) for mice injected with 100 nm SiO_2 nanoshells intravenously at 150 mg/kg is shown in Table 3.1. All values appeared to be within the reference range except a somewhat lowered platelet count. This indicates that the hollow silica shells used in this study have minimal toxicity even at very high intravenous doses. These results agree with previous reports as well as literature for similar materials.[52, 54, 55, 62, 76] Because the systematic toxicity from intra-tumoral injection is much lower than intravenous injection, this test is expected to be a good representation of the safety of these materials as used.

3.9 Acknowledgments

Chapters Three, in full, was published in Applied Surface Science as follows: Garcia Badaracco A, Ward E, Barback C, Yang J, Wang J, Huang CH, Kim M, Wang Q, Nam S, Delong J, Blair S, Trogler W, Kummel A. “Indocyanine green modified silica shells for colon tumor marking”. Applied Surface Science, 2020. Minor changes to the text and figures have been made.

3.10 Figures and Tables

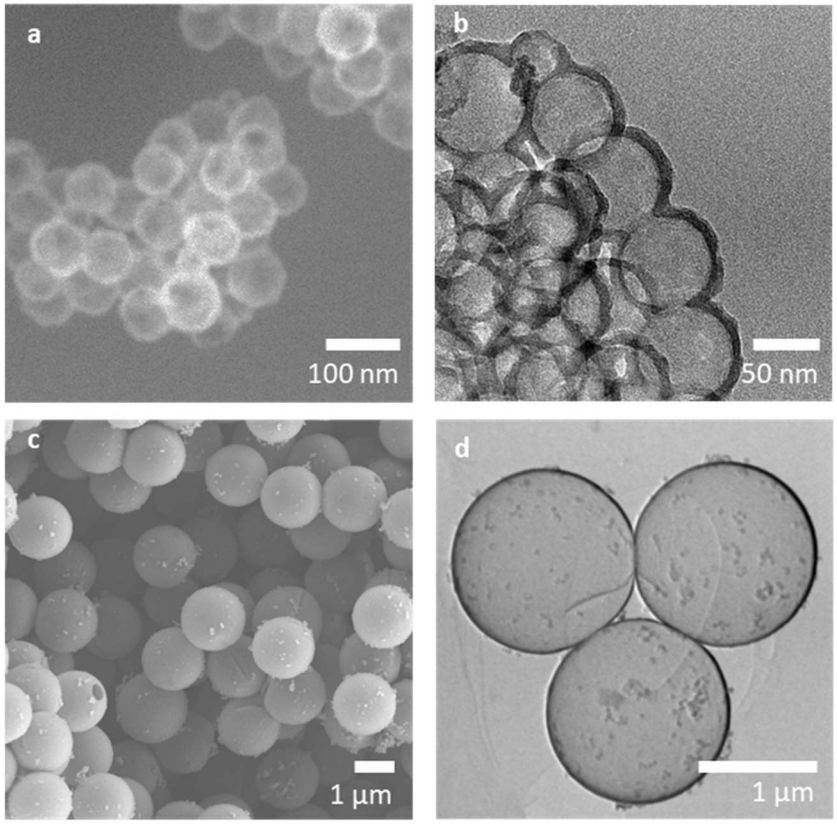

Figure 3.1 Representative EM images of uncoated SiO_2 nanoshells**.** (a) SEM images of 100 nm of hollow SiO_2 nanoshells showing uniform diameter shells and (b) TEM images of the 100 nm SiO_2 nanoshells. 100 nm nanoshells have thin walls (dark, dense region) along with hollow interior space (light region). The walls on the 100nm nanoshells exhibit some non-uniformity relative to the diameter of the particles. (c) SEM images of 2 µm hollow SiO_2 microshells. 2 µm microshells have uniform diameters and, unlike 100 nm nanoshells, have some colloidal silica on the surface. (d) TEM images of the 2 µm microshells showing very uniform thin shell walls relative to the particle diameter.

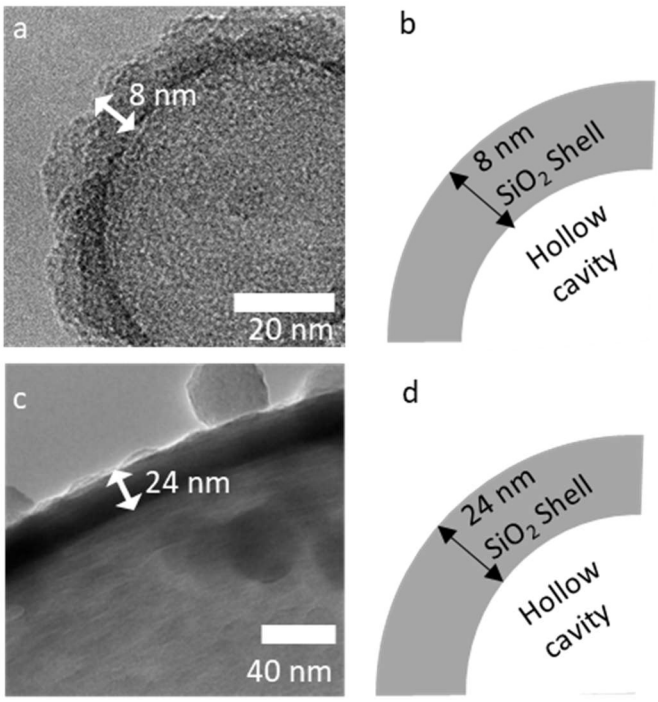

Figure 3.2 TEM images of SiO_2 nanoshell walls. (a) TEM image of uncoated 100 nm nanoshells showing an SiO_2 thickness of approximately 8 nm and (b) schematic representation of the TEM image to aid understanding of the layers and relation to the hollow space. (c) TEM image of an uncoated shell for a 2 μm shell with an SiO_2 layer that is about 24 nm thick, (d) schematic of the TEM image showing the relative position of the hollow cavity inside the shell.

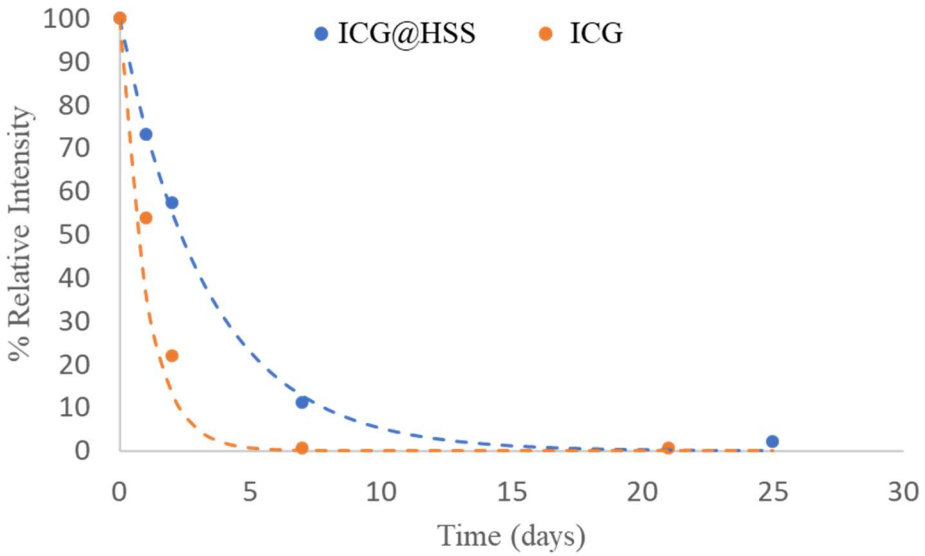

Figure 3.3 Chemical stability of ICG/HSS in water. ICG coated 100 nm silica shells were suspended in water at 0.05 mg/mL to monitor degradation of ICG dye loaded onto the shells. ICG dye of roughly the same ICG concentration (2 µg/mL) was used as a control. Adsorption onto the shell improved the $t_{1/2}$ from 16.6 h^{-1} for free ICG dye to 56.4 h^{-1} for the ICG adsorbed onto the shells. Despite this, both ICG dye and ICG dye on shells degrade in water. The main role of the shell is to localize the dye at the injection site.

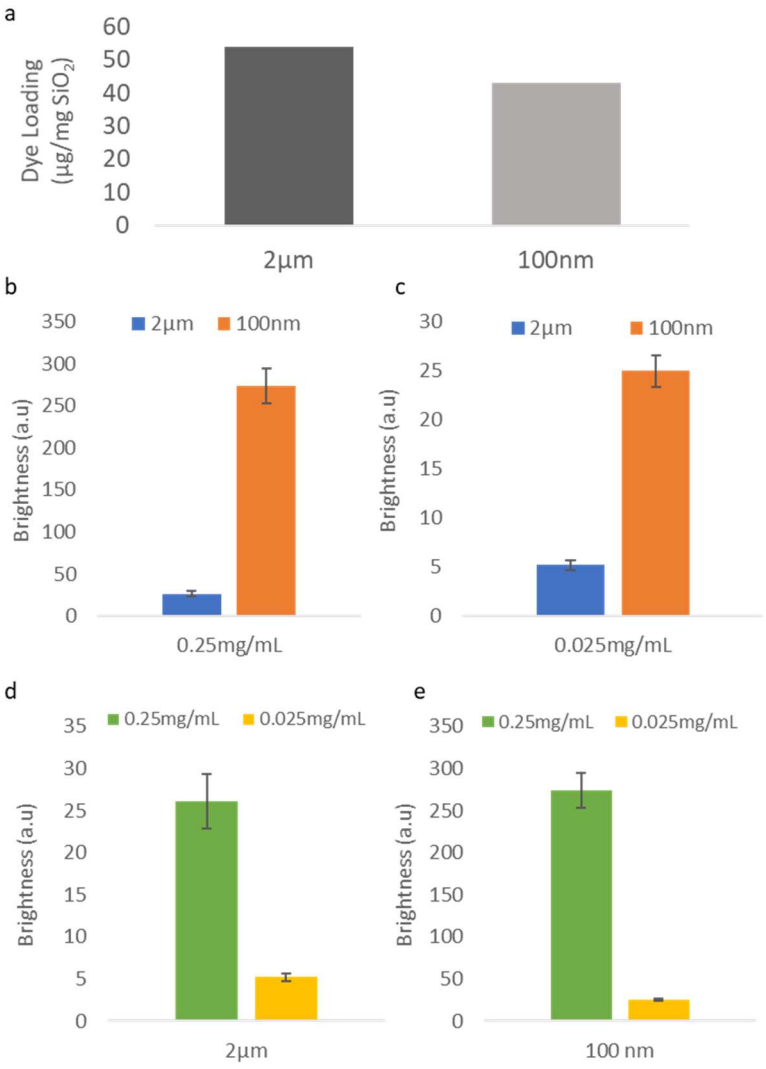

Figure 3.4 Brightness of 100 nm and 2um ICG coated shells**.** (a) Comparison of dye loading between 100 nm nanoshells and 2 µm microshells. Dye loading was measured by suspending the ICG coated shells in water at 0.1mg/mL and measuring absorption against a free ICG dye calibration curve. Loading was found to be 54 µg/mg for 2 µm shells and 43 µg/mg for 100 nm shells. (b) Comparison of fluorescent emission intensity at 0.25 mg/mL SiO_2 mass concentration. 100 nm nanoshells are 10x brighter than the larger 2 µm shells, despite similar bulk ICG concentration (c) Comparison of fluorescent emission intensity at 0.25 mg/mL SiO_2 mass concentration. 100 nm shells are 5x brighter than the 2 µm shells. (d) Comparison between 0.25 mg/mL and 0.025 mg/mL for 2 µm shells. 2 µm shells show a 5x increase in signal strength with a 10x increase in in microshell concentration, suggesting possible self-quenching. (e) Comparison between 0.25 mg/mL and 0.025 mg/mL for 100 nm shells. 100 nm nanoshells exhibit 10x brightness with 10x concentration increase, a linear increase. Raw images for this data are shown in Figure 3.5.

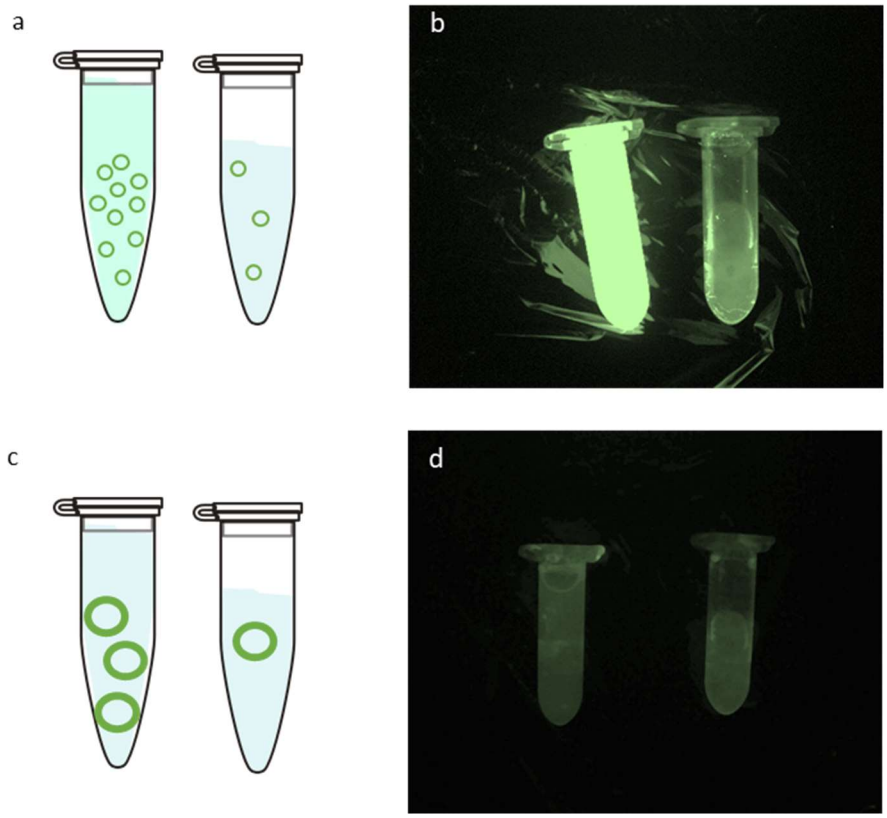

Figure 3.5 NIR images of ICG coated silica shells**.** (a) Schematic of 100 nm nanoshells suspended at 0.25 mg/mL (left) and 0.025 mg/mL (right), (b)Fluorescent IR image of 100 nm nanoshells at 0.25 mg/mL vs 0.025 mg/mL; note 0.25 mg/mL is significantly brighter. (c) Schematic of 2 μm microshells suspended at 0.25 mg/mL (left) and 0.025 mg/mL (right), (d) Fluorescent IR image of 2 μm microshells of 0.25 mg/mL vs 0.025 mg/mL; note the microshells appear to self-quench with little change in brightness vs concentration, Comparing (b) and (d), it can be observed that 100 nm is considerably brighter than 2um. Images taken with IR camera at 200 ms exposure time. Images are uniformly brightness enhanced and recolorized for viewing purposes.

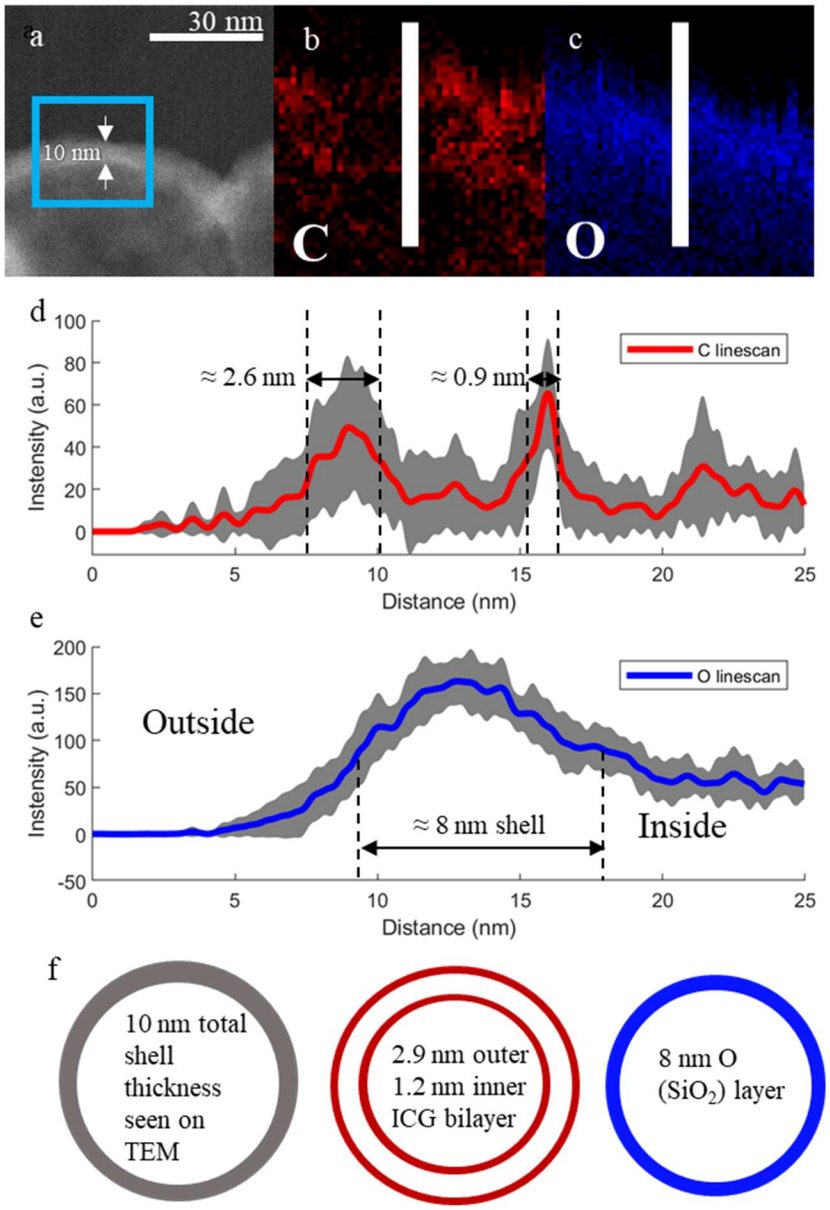

Figure 3.6. TEM-EELS elemental mapping for 100 nm nanoshells**.** (a) TEM image of ICG coated 100 nm shell with the TEM-EELS mapping region highlighted in the blue box and shell thickness of 10 nm measured between the white bars; (b) Elemental map of C on the shell wall by TEM EELS; (c) Elemental map of O on shell wall. The linescan area analyzed is represented by the white bar. (d) The averaged linescan of C on shell wall. A ≈ 2.6 nm exterior ICG layer and 0.9nm interior ICG layer can be seen; (e) Linescan of O on shell wall. Gray areas around the linescans represent standard deviations. Repeat linescans of a 9 nm wide section of shell in the middle of the images were used for averaging as well as calculation of standard deviations. (f) Schematic subdividing the shell wall into an external 2.6 nm ICG coating, the intact 8 nm SiO_2 shell and an internal 0.9 nm ICG coating.

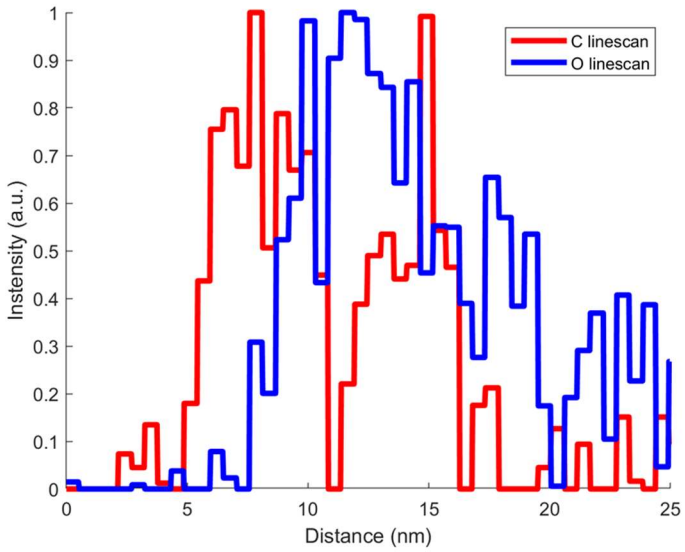

Figure 3.7 Single pixel linescan of 100 nm ICG coated shells. Replot of data in Figure 3.4de showing a linescan of a single pixel (corresponding to 0.4 nm) without averaging or pre-processing. Despite the lower resolution of a single scan, the bimodal distribution of ICG with on both sides of the shell can still be observed.

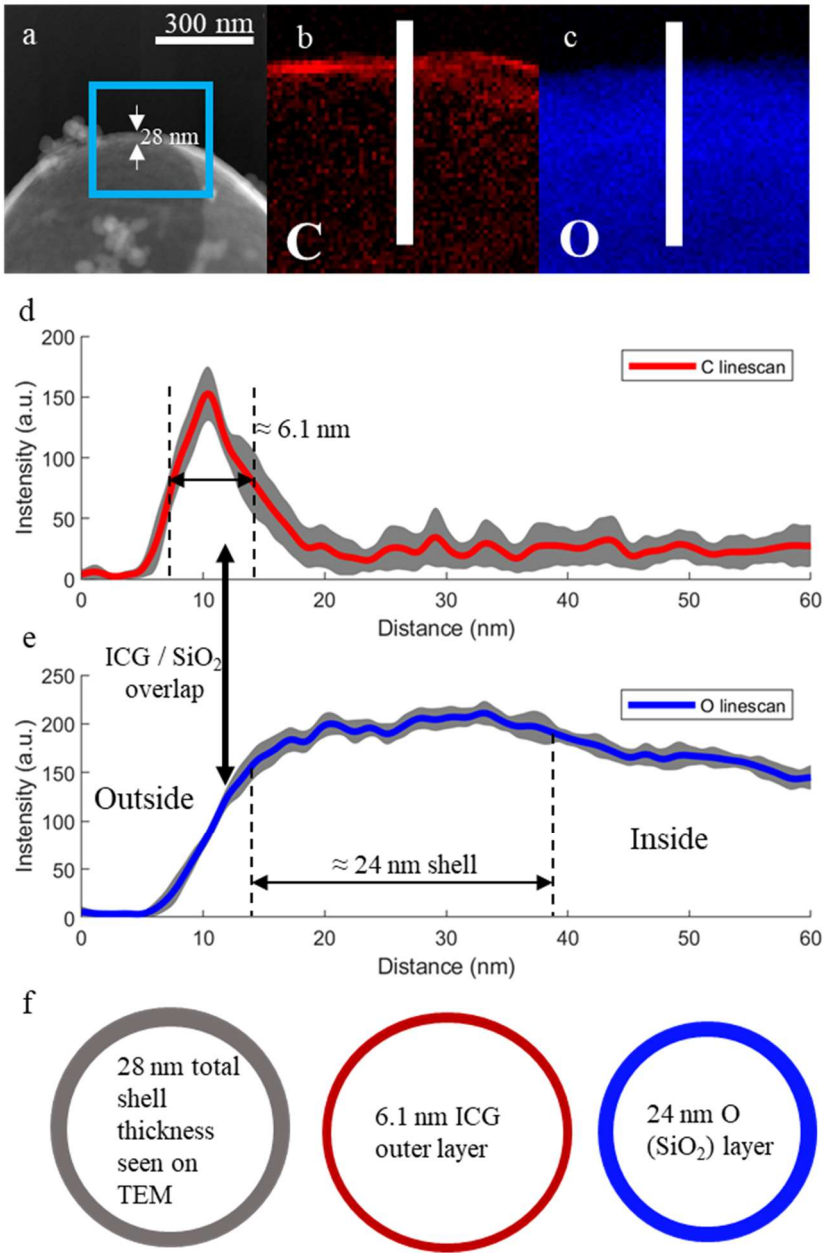

Figure 3.8. TEM-EELS mapping for 2 µm microshells. (a) TEM image of ICG coated 2 µm shell with the TEM-EELS mapping region highlighted in the blue box and shell thickness of 28 nm measured between the white bars; (b) Elemental map of C on the shell wall by TEM EELS; (c) Elemental map of O on shell wall. The linescan area analyzed is represented by the white bar. (d) Averaged linescan of C on shell wall. Unlike the smaller 100 nm shells, 2 µm shells only have an outer ICG layer, of about 6.1 nm. Gray areas around the linescans represent standard deviations. Repeat linescans of a 35 nm wide section of shell in the middle of the images were used for averaging as well as calculation of standard deviations. (f) Schematic subdividing the shell wall into an external 6.1 nm ICG coating and the intact 24 nm SiO_2 shell, with no interior ICG layer visible.

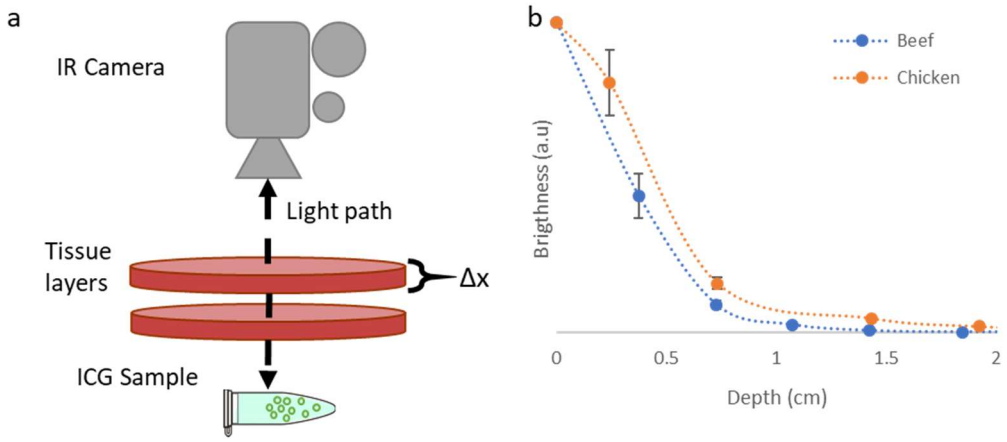

Figure 3.9 Tissue penetration of 100 nm**.** (a) Schematic describing the experimental setup used to test tissue penetration *ex vivo*. An Eppendorf tube was placed a fixed distance from an IR camera, and then thin layers of tissue are placed in the path of the illumination beam. (b) Intensity decay profile using chicken or beef as phantom tissue. Visibility was observed to be up to ≈ 1.5 cm using chicken and ≈ 1 cm using beef. Sample images from the stack shown in (a) are available in Figure 14.

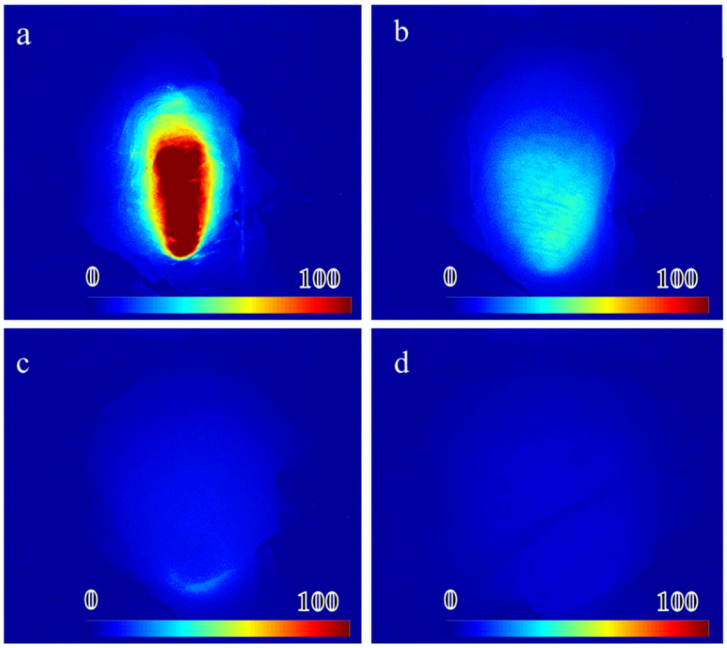

Figure 3.10 Sample images from stacks in Figure 3.9. (a) Single layer (0.242 cm), (b) two layers (0.73 cm), (c) three layers (1.44 cm), and (d) four layers (1.92 cm) of chicken breast tissue layered on top of an Eppendorf tube filled with 100 nm ICG coated nanoshells suspended at 0.25 mg/mL in DI water. Images are artificially colored.

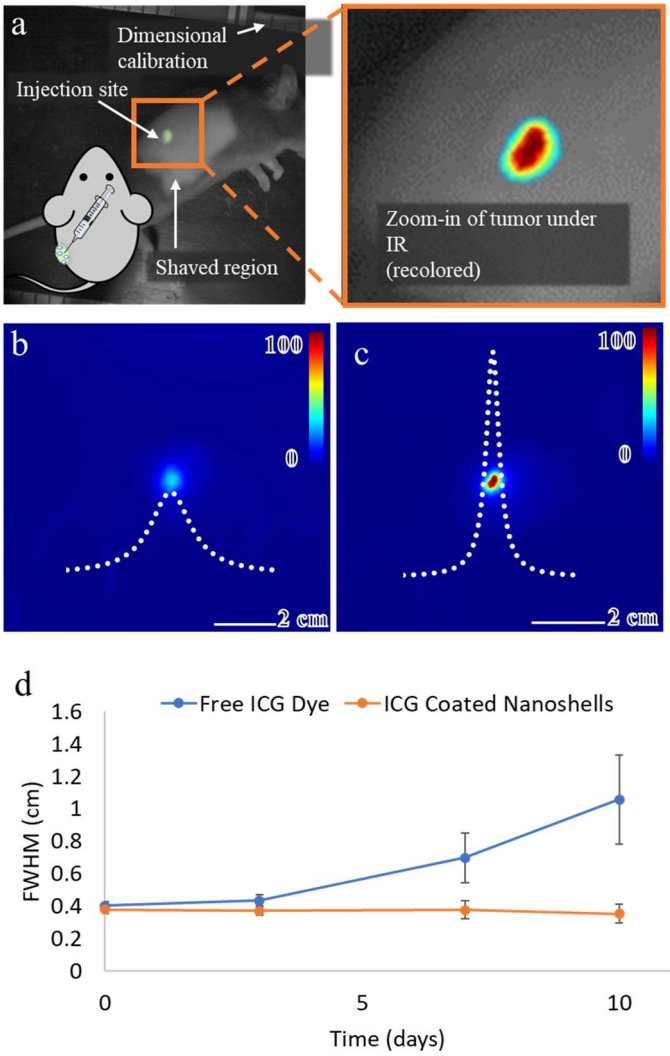

Figure 3.11 Changes in emission profile over time of injection into mice tumors. (a) Visible light image of mouse during IR imaging. The green area is the injection site. The region surrounding the injection site was kept shaved to avoid signal loss due to hair growth during the experiment. The zoomed in panel shows how the NIR images in (b) and (c) relate to the injection site. (b) Emission profile for free ICG dye at day 10. The emission is diffuse and the peak is low in intensity. (c) Emission profile of 100 nm ICG coated nanoshells at day 10. The emission is highly localized, with a clearly delaminated injection region. The Cauchy PDF line of best fit is shown in dotted white. Lines of best fit are enlarged for viewing and are not to scale. (d) Evolution of the FWHM of the emission profile over time. Free ICG dye diffuses through tissue, increasing the FWHM of the emission while ICG coated nanoshells maintain the same emission profile. At day 10, free ICG emission profiles are broader than that of coated shells ($p<0.05$).

Table 3.1 CBC for mice injected with 100 nm SiO_2 nanoshells. Healthy 6-8-week-old female BALB/c mice (n=3) were injected with 150 mg/kg plain 100 nm SiO_2 nanoshells to measure systematic toxicity. 24 hours after injection, 400 uL of blood was collected and a CBC analysis was performed. All values appeared to be within the reference range except a somewhat lowered platelet count.

	Reference Range	**100nm SiO_2 Shells**	**Units**
WBC	1.8-10.7	2.78 ± 0.7	$x10^3/\mu L$
RBC	6.36-9.42	9.06 ± 0.36	$x10^6/\mu L$
HCT	35.1-45.4	51.5 ± 2.46	%
MCV	45.4-60.3	56.83 ± 1.37	fL
MCH	14.1-19.3	15.77 ± 0.5	Pg
MCHC	30.2-34.2	27.73 ± 1.21	g/dL
Platelet	592-2972	246 ± 80.73	$x10^3/\mu L$
Neutrophils	0.1-2.4	1.47 ± 0.4	count/µL
% Neutrophils	Not available	43.33 ± 9.45	%
Lymphocytes	0.9-9.3	1.02 ± 0.42	count/µL
% Lymphocytes	Not available	51.33 ± 8.08	%
Monocytes	0.0-0.4	0.21 ± 0.11	count/µL
Eosinophil Count	0.0-0.2	0.06 ± 0.08	count/µL
Basophils Count	0.0-0.2	0.03 ± 0.04	count/µL
Hemoglobin	11.0-15.1	14.3 ± 1	g/dL
RDW	12.4-27.0	17.57 ± 0.55	%
MPV	5.0-20.0	5.53 ± 0.31	fL

All measurements are shown are mean ± standard deviation.

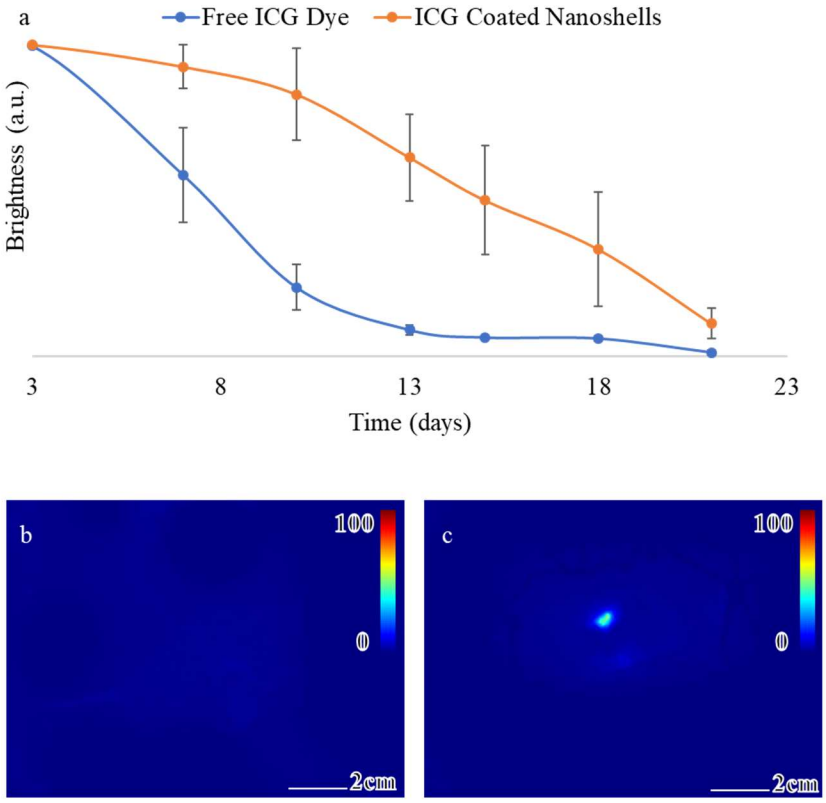

Figure 3.12 In vivo temporal stability of ICG coated nanoshells. (a) Peak NIR emission intensity vs time for 100 nm nanoshells and free ICG dye. ICG coated 100 nm nanoshells and free ICG dye controls were injected into the tumors of mice and imaged at 1000ms exposure over the course of 21 days. Free ICG dye clears from injection site faster than ICG coated shells. For days between 7 and 15 ICG coated shells are brighter ($p<0.05$). (b) Free ICG dye at 1000 ms exposure on day 21. This image confirms that ICG alone no longer shows any signal. (c) 100 nm nanoshells at 1000 ms exposure on day 21. ICG coated nanoshells exhibit a strong emission that makes it very easy to locate the injection site up to day 21 in some mice.

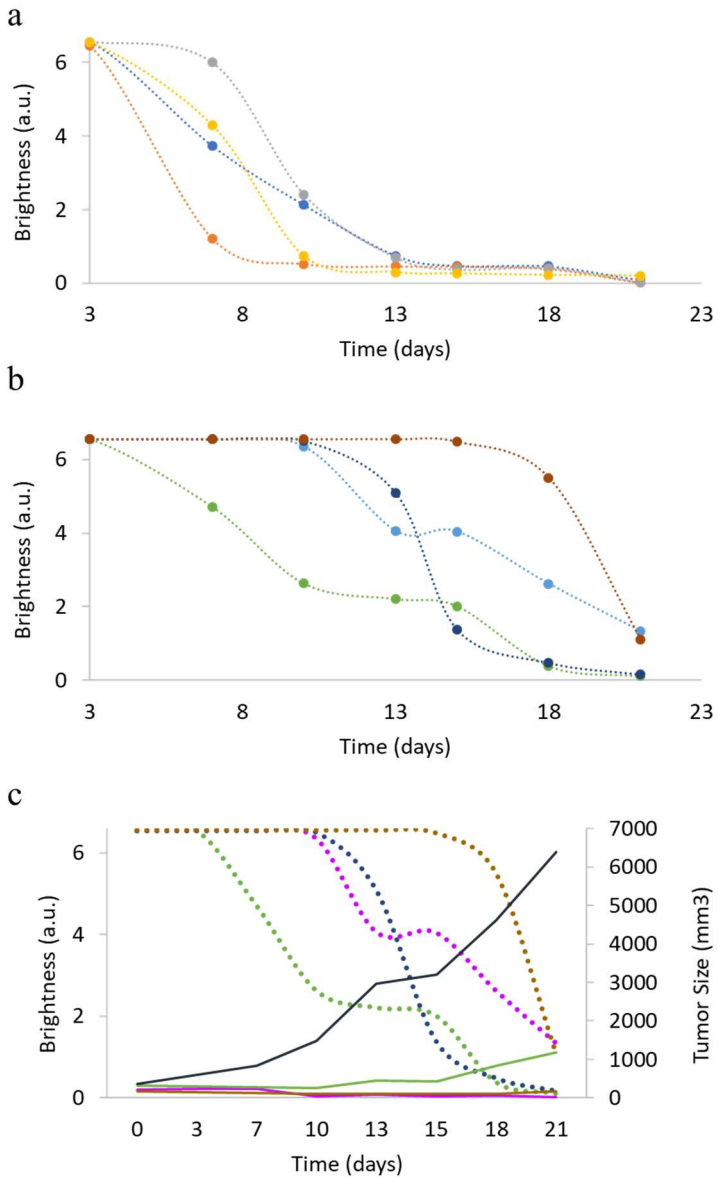

Figure 3.13 Variability of signal over time for individual mouse. Replotting of data shown in Figure 3.12a showing individual time series for each mouse injected with (a) free ICG dye or (b) ICG dye coated 100 nm silica nanoshells. (c) IR Fluorescence of ICG coated nanoshell (dashed lines) and tumor size (corresponding solid lines of same color) vs time for ICG coated nanoshells group. Data is consistent with a strong relationship between drop in signal and tumor size increase.

CHAPTER FOUR

Conclusions

4.1 Conclusions

While free ICG dyes have been proposed for use in tumor marking, free ICG dye still suffers from diffusion through tissue leading to shorter imaging persistence, thereby reducing the accuracy of tumor localization over time. Silica nanoshells were used as a potential carrier for ICG free dyes in order to securely anchor the dye to the injection site and shield the ICG dye from interaction with serum proteins and other biological factors that could reduce emission or degrade the dye.

Bright ICG-based tumor markers were synthesized by non-covalently bonding ICG to the surface of hollow silica microshells and nanoshells using electrostatic attraction between the negatively charged sulfonic groups on ICG molecule and the positively charged amine group on the surface of silica shells. Elemental mapping with TEM-EELS showed dual thin layers (< 3 nm) of dye on the inside and outside of the 100 nm nanoshells greatly enhances emission brightness compared to a thicker exterior coating on larger 2 μm microshells. This effect is consistent with avoiding self-quenching from formation of energy traps, as has been observed with high local concentrations of dye on shell surfaces.

In vitro and in vivo studies documented that these ICG coated 100 nm silica nanoshells can be observed by NIR fluorescence when injected at 1 cm depth into tissue and have a persistent bright signal that lasts over 10 days, with no observable diffusion through tissues. On day 10, the ICG coated nanoshells were significantly brighter than free ICG dye, which had lost significant amount of signal and diffused to the surrounding tissue.

The ICG/HSS hybrid present in this study demonstrates a new class of method for local delivery of dyes with improvement imaging ability and safety profile.

4.2 Acknowledgments

Chapters Four, in full, was published in Applied Surface Science as follows: Garcia Badaracco A, Ward E, Barback C, Yang J, Wang J, Huang CH, Kim M, Wang Q, Nam S, Delong J, Blair S, Trogler W, Kummel A. “Indocyanine green modified silica shells for colon tumor marking”. Applied Surface Science, 2020. Minor changes to the text and figures have been made.

REFERENCES

1. *What Is Cancer?*, in *About Cancer*. 2018, National Cancer Institute, National Institute of Health.
2. *Cancer Statistics*, in *About Cancer*. 2018, National Cancer Institute, National Institute of Health.
3. Greenwald, P., *Colon cancer overview.* Cancer, 1992. **70**(S3): p. 1206-1215.
4. *Cancer Stat Facts: Colorectal Cancer*, in *Cancer Statistics Reports on Cancer*. 2018, National Cancer Institute, National Institute of Health.
5. Acuna, S.A., M. Elmi, P.S. Shah, N.G. Coburn, and F.A. Quereshy, *Preoperative localization of colorectal cancer: a systematic review and meta-analysis.* Surgical endoscopy, 2017. **31**(6): p. 2366-2379.
6. Vogel, J.D., C. Eskicioglu, M.R. Weiser, D.L. Feingold, and S.R. Steele, *The American Society of Colon and Rectal Surgeons clinical practice guidelines for the treatment of colon cancer.* Diseases of the Colon & Rectum, 2017. **60**(10): p. 999-1017.
7. Adler, D.G., *Tattooing and other methods for localizing gastrointestinal lesions*, in *UpToDate*, T.W. Post, Editor. 2020: Waltham, MA.
8. GI Supply, I., *A Gastroenterologist's Guide to Endoscopic Tattooing Methods*. 2018.
9. Elarini, T., S.D. Wexner, and G.A. Isenberg, *The need for standardization of colonoscopic tattooing of colonic lesions.* Diseases of the Colon & Rectum, 2015. **58**(2): p. 264-267.
10. Munegato, G., V.M. De, M. di Visconte Schiano, S. Salemi, S. Barbaresco, and G. Mazzarolo, *The diagnosis of non-palpable lesions in laparoscopic surgery of the colon.* Chirurgia italiana, 2003. **55**(5): p. 657-661.
11. Yeung, J., C. Maxwell-Armstrong, and A. Acheson, *Colonic tattooing in laparoscopic surgery–making the mark?* Colorectal Disease, 2009. **11**(5): p. 527-530.
12. Group, C.C.L.o.O.R.S., *Laparoscopic surgery versus open surgery for colon cancer: short-term outcomes of a randomised trial.* The lancet oncology, 2005. **6**(7): p. 477-484.
13. *Laparoscopic surgery*, in *MedlinePlus*, B. Conaway, Editor. 2019, National Library of Medicine: Bethesda (MD).
14. Escobedo, J.O., O. Rusin, S. Lim, and R.M. Strongin, *NIR dyes for bioimaging applications.* Current opinion in chemical biology, 2010. **14**(1): p. 64-70.
15. Alander, J.T., I. Kaartinen, A. Laakso, T. Pätilä, T. Spillmann, V.V. Tuchin, M. Venermo, and P. Välisuo, *A review of indocyanine green fluorescent imaging in surgery.* Journal of Biomedical Imaging, 2012. **2012**: p. 7.
16. Fernandez, L.M., R.N.M. Ibrahim, I. Mizrahi, G. DaSilva, and S.D. Wexner, *How accurate is preoperative colonoscopic localization of colonic neoplasia?* Surgical endoscopy, 2018: p. 1-6.
17. Liu, Z., J. Liu, F.S. Chan, M.K. Li, and J.K. Fan, *Intraoperative colonoscopy in laparoscopic colorectal surgery: A review of recent publications.* Asian journal of endoscopic surgery, 2020. **13**(1): p. 19-24.

18. Brar, T.S. and P.V. Draganov, *Endoscopic Tattooing: From Blue to Black.* ACG case reports journal, 2016. **3**(4).

19. Lee, J.G., A.H. Low, and J.W. Leung, *Randomized comparative study of indocyanine green and India ink for colonic tattooing: an animal survival study.* J Clin Gastroenterol, 2000. **31**(3): p. 233-6.

20. Miyoshi, N., M. Ohue, S. Noura, M. Yano, Y. Sasaki, K. Kishi, T. Yamada, I. Miyashiro, H. Ohigashi, H. Iishi, O. Ishikawa, and S. Imaoka, *Surgical usefulness of indocyanine green as an alternative to India ink for endoscopic marking.* Surg Endosc, 2009. **23**(2): p. 347-51.

21. Aboosy, N., C. Mulder, F.J. Berends, J. Meijer, and A. Sorge, *Endoscopic tattoo of the colon might be standardized to locate tumors intraoperatively.* Rom J Gastroenterol, 2005. **14**(3): p. 245-248.

22. Kim, S.H., J. Milsom, J. Church, K. Ludwig, A. Garcia-Ruiz, J. Okuda, and V. Fazio, *Perioperative tumor localization for laparoscopic colorectal surgery.* Surgical endoscopy, 1997. **11**(10): p. 1013-1016.

23. Cho, Y.B., W.Y. Lee, H.R. Yun, W.S. Lee, S.H. Yun, and H.-K. Chun, *Tumor localization for laparoscopic colorectal surgery.* World journal of surgery, 2007. **31**(7): p. 1491-1495.

24. Zafar, H.M., J. Yang, K. Armstrong, and P. Groeneveld, *Cost differences after initial CT colonography versus optical colonoscopy in the elderly.* Academic radiology, 2015. **22**(7): p. 807-813.

25. Mettler Jr, F.A., W. Huda, T.T. Yoshizumi, and M. Mahesh, *Effective doses in radiology and diagnostic nuclear medicine: a catalog.* Radiology, 2008. **248**(1): p. 254-263.

26. Coman, E., L.J. Brandt, S. Brenner, M. Frank, B. Sablay, and B. Bennett, *Fat necrosis and inflammatory pseudotumor due to endoscopic tattooing of the colon with india ink.* Gastrointest Endosc, 1991. **37**(1): p. 65-8.

27. Gianom, D., A. Hollinger, and H.P. Wirth, *Intestinal perforation after preoperative colonic tattooing with India ink.* Swiss Surg, 2003. **9**(6): p. 307-10.

28. Watanabe, M., A. Tsunoda, K. Narita, M. Kusano, and M. Miwa, *Colonic tattooing using fluorescence imaging with light-emitting diode-activated indocyanine green: a feasibility study.* Surg Today, 2009. **39**(3): p. 214-8.

29. Luigiano, C., F. Ferrara, C. Morace, B. Mangiavillano, C. Fabbri, V. Cennamo, M. Bassi, C. Virgilio, and P. Consolo, *Endoscopic Tattooing of Gastrointestinal and Pancreatic Lesions.* Advances in Therapy, 2012. **29**(10): p. 864-873.

30. Bang, C.S., Y.S. Kim, G.H. Baik, and S.H. Han, *Colonic Abscess Induced by India Ink Tattooing.* The Korean Journal of Gastroenterology, 2014. **64**(1): p. 45.

31. Nagata, J., Y. Fukunaga, T. Akiyoshi, T. Konishi, Y. Fujimoto, S. Nagayama, N. Yamamoto, and M. Ueno, *Colonic Marking With Near-Infrared, Light-Emitting, Diode-Activated Indocyanine Green for Laparoscopic Colorectal Surgery.* Dis Colon Rectum, 2016. **59**(2): p. e14-8.

32. Schönbächler, A., O. Glaied, J. Huwyler, M. Frenz, and U. Pieles, *Indocyanine green loaded biocompatible nanoparticles: Stabilization of indocyanine green (ICG) using biocompatible silica-poly(ε-caprolactone) grafted nanocomposites.* Journal of Photochemistry and Photobiology A: Chemistry, 2013. **261**: p. 12-19.

33. Lv, R., D. Wang, L. Xiao, G. Chen, J. Xia, and P.N. Prasad, *Stable ICG-loaded upconversion nanoparticles: silica core/shell theranostic nanoplatform for dual-modal upconversion and photoacoustic imaging together with photothermal therapy.* Scientific Reports, 2017. **7**(1): p. 15753.

34. Lee, C.H., S.H. Cheng, Y.J. Wang, Y.C. Chen, N.T. Chen, J. Souris, C.T. Chen, C.Y. Mou, C.S. Yang, and L.W. Lo, *Near-Infrared Mesoporous Silica Nanoparticles for Optical Imaging: Characterization and In Vivo Biodistribution.* Advanced Functional Materials, 2009. **19**(2): p. 215-222.

35. Benson, R. and H. Kues, *Fluorescence properties of indocyanine green as related to angiography.* Physics in medicine and biology, 1978. **23**(1): p. 159.

36. Malicka, J., I. Gryczynski, C.D. Geddes, and J.R. Lakowicz, *Metal-enhanced emission from indocyanine green: a new approach to in vivo imaging.* Journal of biomedical optics, 2003. **8**(3): p. 472-478.

37. Landsman, M., G. Kwant, G. Mook, and W. Zijlstra, *Light-absorbing properties, stability, and spectral stabilization of indocyanine green.* Journal of applied physiology, 1976. **40**(4): p. 575-583.

38. Li, X., B. Beauvoit, R. White, S. Nioka, B. Chance, and A.G. Yodh. *Tumor localization using fluorescence of indocyanine green (ICG) in rat models*. in *Optical Tomography, Photon Migration, and Spectroscopy of Tissue and Model Media: Theory, Human Studies, and Instrumentation*. 1995. International Society for Optics and Photonics.

39. Taichman, G.C., P.J. Hendry, and W.J. Keon, *The use of cardio-green for intraoperative visualization of the coronary circulation: evaluation of myocardial toxicity.* Texas Heart Institute Journal, 1987. **14**(2): p. 133.

40. de la Zerda, A., S. Bodapati, R. Teed, S.Y. May, S.M. Tabakman, Z. Liu, B.T. Khuri-Yakub, X. Chen, H. Dai, and S.S. Gambhir, *Family of enhanced photoacoustic imaging agents for high-sensitivity and multiplexing studies in living mice.* ACS nano, 2012. **6**(6): p. 4694-4701.

41. Yang, X., E.W. Stein, S. Ashkenazi, and L.V. Wang, *Nanoparticles for photoacoustic imaging.* Wiley interdisciplinary reviews: nanomedicine and nanobiotechnology, 2009. **1**(4): p. 360-368.

42. Wang, H., C. Liu, X. Gong, D. Hu, R. Lin, Z. Sheng, C. Zheng, M. Yan, J. Chen, and L. Cai, *In vivo photoacoustic molecular imaging of breast carcinoma with folate receptor-targeted indocyanine green nanoprobes.* Nanoscale, 2014. **6**(23): p. 14270-14279.

43. Chen, W.R., R.L. Adams, A.K. Higgins, K.E. Bartels, and R.E. Nordquist, *Photothermal effects on murine mammary tumors using indocyanine green and an 808-nm diode laser: an in vivo efficacy study.* Cancer letters, 1996. **98**(2): p. 169-173.

44. Yu, J., D. Javier, M.A. Yaseen, N. Nitin, R. Richards-Kortum, B. Anvari, and M.S. Wong, *Self-assembly synthesis, tumor cell targeting, and photothermal capabilities of antibody-coated indocyanine green nanocapsules.* Journal of the American Chemical Society, 2010. **132**(6): p. 1929-1938.

45. Yu, J., M.A. Yaseen, B. Anvari, and M.S. Wong, *Synthesis of near-infrared-absorbing nanoparticle-assembled capsules.* Chemistry of materials, 2007. **19**(6): p. 1277-1284.

46. Abels, C., S. Karrer, W. Bäumler, A. Goetz, M. Landthaler, and R. Szeimies, *Indocyanine green and laser light for the treatment of AIDS-associated cutaneous Kaposi's sarcoma.* British journal of cancer, 1998. **77**(6): p. 1021-1024.

47. Desmettre, T., J. Devoisselle, and S. Mordon, *Fluorescence properties and metabolic features of indocyanine green (ICG) as related to angiography.* Survey of ophthalmology, 2000. **45**(1): p. 15-27.

48. e Sousa, A.R., J. Martinho, F. Baros, and J. André, *Self-quenching of azulene fluorescence in cyclohexane.* Journal of Photochemistry and Photobiology A: Chemistry, 1994. **83**(3): p. 199-203.

49. Mok, H., H. Jeong, S.-J. Kim, and B.H. Chung, *Indocyanine green encapsulated nanogels for hyaluronidase activatable and selective near infrared imaging of tumors and lymph nodes.* Chemical Communications, 2012. **48**(69): p. 8628-8630.

50. Saxena, V., M. Sadoqi, and J. Shao, *Enhanced photo-stability, thermal-stability and aqueous-stability of indocyanine green in polymeric nanoparticulate systems.* Journal of Photochemistry and Photobiology B: Biology, 2004. **74**(1): p. 29-38.

51. Martinez, H.P., Y. Kono, S.L. Blair, S. Sandoval, J. Wang-Rodriguez, R.F. Mattrey, A.C. Kummel, and W.C. Trogler, *Hard shell gas-filled contrast enhancement particles for colour Doppler ultrasound imaging of tumors.* MedChemComm, 2010. **1**(4): p. 266-270.

52. Liberman, A., H.P. Martinez, C.N. Ta, C.V. Barback, R.F. Mattrey, Y. Kono, S.L. Blair, W.C. Trogler, A.C. Kummel, and Z. Wu, *Hollow silica and silica-boron nano/microparticles for contrast-enhanced ultrasound to detect small tumors.* Biomaterials, 2012. **33**(20): p. 5124-5129.

53. Ozkan, S.A. and A. Shah, *New Developments in Nanosensors for Pharmaceutical Analysis*. 2019: Academic Press.

54. Liberman, A., N. Mendez, W.C. Trogler, and A.C. Kummel, *Synthesis and surface functionalization of silica nanoparticles for nanomedicine.* Surface science reports, 2014. **69**(2): p. 132-158.

55. Liberman, A., Z. Wu, C.V. Barback, R. Viveros, S.L. Blair, L.G. Ellies, D.R. Vera, R.F. Mattrey, A.C. Kummel, and W.C. Trogler, *Color doppler ultrasound and gamma imaging of intratumorally injected 500 nm iron–silica nanoshells.* ACS nano, 2013. **7**(7): p. 6367-6377.

56. Ta, C.N., A. Liberman, H.P. Martinez, C.V. Barback, R.F. Mattrey, S.L. Blair, W.C. Trogler, A.C. Kummel, and Z. Wu, *Integrated processing of contrast pulse sequencing ultrasound imaging for enhanced active contrast of hollow gas filled silica nanoshells and microshells.* Journal of Vacuum Science & Technology B, 2012. **30**(2): p. 02C104.

57. Yang, J., J.U. Lind, and W.C. Trogler, *Synthesis of hollow silica and titania nanospheres.* Chemistry of Materials, 2008. **20**(9): p. 2875-2877.

58. Yang, J., J. Wang, C.N. Ta, E. Ward, C.V. Barback, T.-W. Sung, N. Mendez, S.L. Blair, A.C. Kummel, and W.C. Trogler, *Ultrasound Responsive Macrophase-Segregated Microcomposite Films for in Vivo Biosensing.* ACS applied materials & interfaces, 2017. **9**(2): p. 1719-1727.

59. Yang, J., E.P. Ward, T.-W. Sung, J. Wang, C.V. Barback, N. Mendez, S.L. Blair, W.C. Trogler, and A.C. Kummel, *Silica shells/adhesive composite film for color Doppler ultrasound guided needle placement.* ACS Biomaterials Science & Engineering, 2017.

60. Liberman, A., J. Wang, N. Lu, Viveros, A. R.D., C.A., R.F. Mattrey, S.L. Blair, W.C. Trogler, M.J. Kim, and A.C. Kummel, *Mechanically Tunable Hollow Silica Ultrathin Nanoshells for Ultrasound Contrast Agents.* Advanced functional materials, 2015. **25**(26): p. 8.

61. ho Hong, S., H. Kim, and Y. Choi, *Indocyanine green-loaded hollow mesoporous silica nanoparticles as an activatable theranostic agent.* Nanotechnology, 2017. **28**(18): p. 185102.

62. Huang, C.-H., N. Mendez, O.H. Echeagaray, J. Weeks, J. Wang, C.N. Vallez, N. Gude, W.C. Trogler, D.A. Carson, and T. Hayashi, *Conjugation of a Small-Molecule TLR7 Agonist to Silica Nanoshells Enhances Adjuvant Activity.* ACS applied materials & interfaces, 2019. **11**(30): p. 26637-26647.

63. Fickweiler, S., R.-M. Szeimies, W. Bäumler, P. Steinbach, S. Karrer, A.E. Goetz, C. Abels, and F. Hofstädter, *Indocyanine green: intracellular uptake and phototherapeutic effects in vitro.* Journal of Photochemistry and Photobiology B: biology, 1997. **38**(2-3): p. 178-183.

64. Ferrauto, G., F. Carniato, E. Di Gregorio, L. Tei, M. Botta, and S. Aime, *Large photoacoustic effect enhancement for ICG confined inside MCM-41 mesoporous silica nanoparticles.* Nanoscale, 2017. **9**(1): p. 99-103.

65. Quan, B., K. Choi, Y.-H. Kim, K.W. Kang, and D.S. Chung, *Near infrared dye indocyanine green doped silica nanoparticles for biological imaging.* Talanta, 2012. **99**: p. 387-393.

66. Luo, T., P. Huang, G. Gao, G. Shen, S. Fu, D. Cui, C. Zhou, and Q. Ren, *Mesoporous silica-coated gold nanorods with embedded indocyanine green for dual mode X-ray CT and NIR fluorescence imaging.* Optics express, 2011. **19**(18): p. 17030-17039.

67. Altınoğlu, E.I., T.J. Russin, J.M. Kaiser, B.M. Barth, P.C. Eklund, M. Kester, and J.H. Adair, *Near-Infrared Emitting Fluorophore-Doped Calcium Phosphate Nanoparticles for In Vivo Imaging of Human Breast Cancer.* ACS Nano, 2008. **2**(10): p. 2075-2084.

68. Rodriguez, V.B., S.M. Henry, A.S. Hoffman, P.S. Stayton, X. Li, and S.H. Pun, *Encapsulation and stabilization of indocyanine green within poly(styrene-alt-maleic anhydride) block-poly(styrene) micelles for near-infrared imaging.* Journal of Biomedical Optics, 2008. **13**(1): p. 1-10, 10.

69. Beziere, N., N. Lozano, A. Nunes, J. Salichs, D. Queiros, K. Kostarelos, and V. Ntziachristos, *Dynamic imaging of PEGylated indocyanine green (ICG) liposomes within the tumor microenvironment using multi-spectral optoacoustic tomography (MSOT).* Biomaterials, 2015. **37**: p. 415-424.

70. He, Q., Z. Zhang, Y. Gao, J. Shi, and Y. Li, *Intracellular localization and cytotoxicity of spherical mesoporous silica nano-and microparticles.* Small, 2009. **5**(23): p. 2722-2729.

71. Liberman, A., Z. Wu, C.V. Barback, R.D. Viveros, J. Wang, L.G. Ellies, R.F. Mattrey, W.C. Trogler, A.C. Kummel, and S.L. Blair, *Hollow iron-silica nanoshells for enhanced high intensity focused ultrasound.* journal of surgical research, 2014. **190**(2): p. 391-398.

72. Anthony, G.J., K.B. Bader, J. Wang, M. Zamora, A. Ostdiek, T. Antic, S. Krueger, S. Weiss, W.C. Trogler, and S.L. Blair, *MRI-guided transurethral insonation of silica-shell phase-shift emulsions in the prostate with an advanced navigation platform.* Medical physics, 2019. **46**(2): p. 774-788.

73. Saxena, V., M. Sadoqi, and J. Shao, *Degradation kinetics of indocyanine green in aqueous solution.* Journal of pharmaceutical sciences, 2003. **92**(10): p. 2090-2097.

74. Rodriguez, H.B. and E.S. Roman, *Effect of Concentration on the Photophysics of Dyes in Light-Scattering Materials.* Photochemistry and Photobiology, 2013. **89**(6): p. 9.

75. Rodriguez, H.B., M. Mirenda, M.G. Lagorio, and E.S. Roman, *Photophysics at Unusually High Dye Concentrations.* Accounts of Chemical Research, 2019. **52**(1): p. 8.

76. Mendez, N., A. Liberman, J. Corbeil, C. Barback, R. Viveros, J. Wang, J. Wang-Rodriguez, S.L. Blair, R. Mattrey, and D. Vera, *Assessment of in vivo systemic toxicity and biodistribution of iron-doped silica nanoshells.* Nanomedicine: Nanotechnology, Biology and Medicine, 2017. **13**(3): p. 933-942.